UNICA UNIVERSITÀ DEGLI STUDI DI CAGLIARI

This is the Author's [*accepted*] manuscript version of the following contribution:

[Hao Fu, Xiaojun Chen, Wei Wang, Giorgio Pia, Jianliang Zhang, Jinxu Li, Statistical study on the effects of heterogeneous deformation and grain boundary character on hydrogen-induced crack initiation and propagation in twining-induced plasticity steels**,** Corrosion Science, 192, November 2021, 109796]

The publisher's version is available at:
https://doi.org/10.1016/j.corsci.2021.109796

When citing, please refer to the published version.

© <2021>. This manuscript version is made available under the CC-BY-NC-ND 4.0 license https://creativecommons.org/licenses/by-nc-nd/4.0/(opens in new tab/window)

This full text was downloaded from UNICA IRIS https://iris.unica.it/

Statistical study on effects of heterogeneous deformation and grain boundary characteristics on hydrogen-induced cracks initiation and propagation in twining induced plasticity steels

Hao Fu[a], Xiaojun Chen[b], Wei Wang[a], Giorgio Pia[c], Jinxu Li[a*]

[a] *Corrosion and Protection Center, Institute of Advanced Materials and Technology, University of Science and Technology Beijing, Beijing 100083, China*

[b] *Key Laboratory of Tectonics and Petroleum Resources, Ministry of Education, China University of Geosciences, Wuhan 430074, China;*

[c] *Dipartimento di Ingegneria Meccanica, Chimica e dei Materiali, Università degli Studi di Cagliari, via Marengo 2, 09123 Cagliari, Italy*

Abstract

The initiation and propagation of hydrogen-induced cracks (HICs) in twining-induced plasticity (TWIP) steel were quantificationally explored based on the HIC statistics at a macro level and a micro level by slow strain rate tensile (SSRT) with in-situ hydrogen-charging and electron microanalysis. The heterogeneous deformation and grain boundary character determines a HIC initiation. The slip transfer parameter $m' < 0.93$ and the minimum residual Burgers vector of residual dislocations on a grain boundary $br > 0.19$ were the critical condition for HIC initiation. Moreover, HICs prone to initiate and propagate along random grain boundaries (RGBs), while the $\Sigma 3$ grain boundaries and vice.

Key words:

twining induced plasticity steels, hydrogen-induced cracks, statistical analysis, heterogeneous deformation, slip transfer, grain boundary characteristics

1. Introduction

Owing to their excellent comprehensive mechanical properties, twining induced plasticity (TWIP) steel drawn more attention from some industries necessitating strict safety and fuel efficiency regulations, which include the automobile, liquefied natural gas, ship-building and oil exploration industries, etc. [1–3]. TWIP steel is endowed with lightweight materials that is a good candidate for safety structures and impact and wear-resistant parts. However, TWIP steel is prone to hydrogen-induced delayed fracture (HIDF), limiting its application as a safety structural component [4–6]. Combining with our previous and other researchers' studies, the brittle zone of fracture surfaces primarily exhibits the typical intergranular fracture character of TWIP steels after slow strain rate tensile (SSRT) test with in situ hydrogen charging [7–9], which suggests that the occurrence of HIDF is the result of the grain boundary being weakened by hydrogen atoms, i.e. it has grain boundary dependence. Therefore, improving the HIDF resistance by controlling the grain boundary type or grain boundary character distribution (GBCD) is a worthwhile way to study and explore TWIP steels. Generally, grain boundaries can be categorized based on the coincident site lattice (CSL) model [10–12], and the CSL lattice can be defined as the geometrically overlapping lattice points of adjacent grains. Previous work has shown that the free volume in the atomic structure of the CSL grain boundary is small and has a high coincidence site lattice, which can effectively suppress the grain boundary segregation [13,14] and grain boundary diffusion [15]. In early 1984, the concept of "grain boundary design and control" was first proposed by Watanabe [16], and it was later termed as "grain boundary engineering (GBE)". The purpose of

GBE is to improve the material properties related to grain boundaries, such as resistance to intergranular corrosion [17, 18], stress corrosion cracking [19,20] and creep [21], its means is to improve the fraction of low-ΣCSL grain boundaries and control the GBCD in materials. However, the application of GBE to HIDF has so far received little attention. Bechtle et al. [22] reported the hydrogen embrittlement properties of Ni-based alloys by controlling the fraction of different types of grain boundaries. The GBE studies on TWIP steel hydrogen embrittlement have also been limited to the two publications by Kwon et al. [23,24], their results showed that the effect of changing the grain boundary type on the hydrogen embrittlement is equivalent to the effect of adding an aluminum element in the TWIP steels. It is well and propagation until the final fracturing for polycrystalline metal materials with intergranular fractures [25,26]. However, the research on the relationship between the HIC initiation and propagation and the grain boundary characteristics has not yet addressed for TWIP steels. Therefore, exploring the HICs initiation and propagation in relation to the grain boundary types or GBCD has engineering value and academic significance for service life evaluations in hydrogen environments and for HIDF mechanism studies on TWIP steels. HIC initiation was strongly affected by the microstructure (grain orientation, grain boundary characteristics and dislocation configuration, etc.) [27,28], micromechanics (local stress or strain) [29,30], and environmental factors (hydrogen content) [31,32] for polycrystalline metal materials. Regarding HIC initiation in TWIP steels, Koyama et al. [33] found that the configuration character of the deformation twins and the grain boundary or triple junction promote HIC initiation combined with the influence of the hydrogen environment. While exploring the relationship between HIC initiation and microstructures in TWIP/TRIP steels in our previous work [7], we found that the dislocations slip plays a dominant role in HIC initiation at slower strain rates, while the deformation twins dominate the initiation at a higher strain rates during the SSRT with hydrogen charging. This finding indicates that the HIC initiations in TWIP/TRIP steels were caused by hydrogen atom diffusion and enrichment as led by the microstructure evolution, and it depended on the strain rate. Nevertheless, the above studies all reported the influence of microstructure on HICs initiation, and they do not involve the

effect of stress or strain at the micro scale. As we already known, heterogeneous deformation during plastic deformation is a common phenomenon for polycrystalline single-phase metal materials with face-centered structures [34], especially for TWIP steels at a lower strain rate [35]. Heterogeneous deformation shows that the deformation not only varies within the grains but also among grains. The significant gradients in deformation between the grains is expressed as a stress or strain transfer in micromechanics [36,37]. Additionally, the stress or strain transfer between adjacent grains is strongly affected by the grain boundary type [38,39]. More importantly, the stress and strain transfer will also cause hydrogen redistribution when hydrogen is present in the material [40], furthermore, which could further influence the hydrogen-induced damage nucleation. Regarding TWIP steels, heterogeneous deformation is manifested as the dislocation slip or deformation twining transfer occurs within the adjacent grains, which would result in the transfer of strain or stress across the grain boundaries. Researchers have previously reported that TWIP steels enjoyed abundant CSL grain boundaries (e.g., $\Sigma 3$, $\Sigma 9$, etc.) following thermomechanical treatment [23,24]. However, there have been no reports on the effect of heterogeneous deformation characteristics (dislocation slip or deformation twining transfer) on HIC initiation for different grain boundaries types. This behavior can not only cause HIC initiation, but it can also prevent crack initiation to some extent. Therefore, it requires statistical evidence to clearly inform phenomenology at lower scales or deterministic models based on physics, and it fully infers HIC initiation at higher scales due to variability in the microstructure. This information may improve the references for TWIP steel alloy design and optimized heat treatment in a reasonable way. At present, there are relatively few reports on HIC propagation for materials processed by GBE. Traditionally, studies on HIC propagation has been based on the analysis of relatively few grains by electron microscopy with higher spatial-temporal resolution, which prevents the determination of specific grain boundary types and makes it difficult to draw statistical and quantitative conclusions [41,42]. Unless a notched specimen is manually introduced, i.e., sliced by a focused ion beam, the location of the crack propagation is unknown. Therefore, this research usually requires periodic test interruption and careful surface

inspection, which is very time-consuming work. Regarding HIC propagation in TWIP steels, Koyama et al. [33] reported that HICs propagate along grain boundaries or deformation twins. We previously reported that the γ/ε interface with a Nishiyama–Wassermann orientation relationship will hinder HICs propagation [7]. These are all qualitative studies on HIC propagation at the microstructure (interface characteristics) level. Nonetheless, from the macro to the micro scale, the quantitative study of HIC propagation has rarely been reported. Researches, in particular, have sought the correlation between HIC propagation at the macro level (such as the crack size, number and distribution) and the irregular and complicated distribution of grain boundaries at the micro level, and the dependence of statistical laws about HIC propagation according to grain boundary type requires further exploration. The fractal dimension provides a reasonable statistical physical method due to its scale invariance in the quantitative characterization of complex irregular shapes across scales [43–46]. In our previous study, we applied fractal theory to explore the relationship between hydrogen embrittlement susceptibility and complicated intergranular fractures for TWIP steels, and a quantitative relationship between the macroscopic weight loss of the intergranular corrosion and the micro grain boundaries distribution state was successfully constructed as well [8,18]. Unfortunately, as far as the author knows, there have been very few statistical studies of the macroscopic HIC distribution and the grain boundary microstructure that applies fractal theory so far [47,48]. In this study, a systematic evaluation of HIC initiation was performed from a micromechanical (stress or strain) perspective to understand the basic HIDF mechanism and key microstructure parameters for TWIP steels specimens with different grain boundary types to a comprehensive extent. To this end, the dependence of HIC propagation on the grain boundary type has been explored at a macro and micro levels. For this purpose, scanning electron microscopy (SEM), electron backscatter diffraction (EBSD), transmission electron microscopy (TEM) and digital image processing were used to characterize the HICs. The focus of the research is the influence of the slip or deformation twining transfer between adjacent grains and the grain boundary character on HIC initiation as well as the of HICs propagation quantification and statistics.

2. Experiment procedures and statistical calculation method

2.1 Thermal-mechanical treatment process

The TWIP steel composition in the current study was Fe-18Mn-0.6C (Table 1). The test steel was melted in a vacuum induction furnace under argon an atmosphere and then cast into a 21 kg ingot. The ingot was forged into a 900 × 100 × 40 mm3 board after being kept at 1423 K for 1.5 h. A layer of commercial anti-oxidation decarburization coating was evenly painted on the ingot surface before the forging to prevent oxidative decarburization. The forged steel bulks were hot rolled to 3.6 mm (with an opening temperature of 1323 K and a final rolling temperature greater than 1173 K) followed by air-cooling to room temperature and then the surface iron oxide scale was removed by grinding. The GBE design of the test steels will be performed on this basis. First, a set of hot rolled specimens were solution treatment at 1248 K for 10 min, followed by water-cooled to room temperature, which was named G1; second, parts of the G1 specimens were subjected to cold rolling with a 5% thickness reduction and then annealed at 1248 K for 5 min, followed immediately by water-cooling to room temperature, which was called G2. Lastly, another set of hot-rolled specimens were solution treated at 1273 K for 10 min and then water-cooled to room temperature, followed by cold rolling for a 5% of thickness reduction, and these specimens were subjected to anneal at 1248 K for 5 and 7 min, respectively, followed immediately by water cooling to room temperature, and the resulting specimens were named G3 and G4. The detailed heat treatment process is shown in Fig. 1. The entire process was

performed under an argon atmosphere.

2.2 Slow strain rate tensile test

The SSRT test was applied to evaluate the HIDF properties of the TWIP steels in this study. There were two SSRT test environments: air and in situ hydrogen-charging. The test steels were cut into tensile specimens with a gauge size measuring 20 mm (length) × 5 mm (width) × 1.4 mm (thickness) by an applying an electric spark along the rolling direction (specimen drawing as shown in Fig. S1). The tensile specimens were mechanically polished using metallographic sandpaper with a particle size of # 300 to # 5000 in order to reduce the thickness from 1.4 mm to approximately 1.2 mm. The tensile specimens were mechanically polished with a particle size of 1.5 μm before SSRT test to obtain the statistical results of subsequent HICs more accurately. The strain rates of the SSRT test are 1 × 10□ 5 s□ 1 and 1 × 10□ 6 s□ 1, respectively. During the SSRT test, in situ hydrogen-charging was performed at ambient temperature through an electrochemical charging device, which is detailed in previous work [7,8,49]. The hydrogen was continuously introduced into the specimens with 5 A/m2 current density at 3% sodium chloride and 3 g/L ammonium thiocyanate solution, the solution is continuously added to cover the gauge part of the tensile specimens and platinum wire was used as the counter electrode. We used the uniform plastic elongation of the specimens after the SSRT test to characterize the hydrogen embrittlement susceptibility (*Eloss*) as follows:

$$E_{loss} = \frac{E_{U(\text{air})} - E_{U(\text{H})}}{E_{U(\text{air})}}$$

where $E_{U(\mathrm{air})}$ and $E_{U(H)}$ represent the uniform elongation of the hydrogen-free and hydrogen-charging specimens, respectively. Besides, the fraction of brittle area (*AB/T*) is introduced to visualize the effect of hydrogen on the fracture mode, which could also assess hydrogen embrittlement susceptibility:

$$A_{B/T} = \frac{A_B}{A_T} \times 100\%$$

where A_T is the total area of the fracture surface and *AB* is the area of the brittle region. The specific calculation method is in the Supplementary material.

2.3 Microstructure characterization

The four specimens (G1–G4) were mechanically polished using diamond polishing paste with a particle size of 1.5 μm and suspended polishing liquid with a particle size of 0.04 μm after being polished with 300 # to 5000 # metallographic sandpaper. They were then electrolytically polished with 10% perchloric acid + 90% acetic acid. The thickness loss of each specimen is strictly controlled within 3 μm. After electrolytic polishing, the grain boundary characteristic distribution was characterized using a focused ion beam field emission electron microscope (Tescan mira 3 LMH) with an electron backscatter EBSD probe (Symmetry). The working voltage was 20 kV, the working distance was 17.0 mm, the scan step was 45 nm and the data processing software was Channel 5 and professional documentation [50]. The grain boundary of $1 < \Sigma \leq 29$ is defined as low-ΣCSL grain boundary in this study [51]. The CSL misorientation was defined according to Brandon's [52] criterion, $\Delta\theta_{\max} = 15° \Sigma^{-1/2}$.

The austenitic phase stability of four specimens before and after SSRT is measured by XRD (UItima IV). The target material is a copper target, the wavelength is 1.5406 Å, the scanning speed is 20◦/min and the scanning range is 40–100◦. The fracture surface was observed by field emission SEM after SSRT with in situ hydrogen-charging. The working voltage was 20 kV, and the working distance was 12–13 mm. The crystallographic information on the secondary microcrack initiation and expansion on the gauge part of the tensile specimen was also tested by EBSD (The specific parameters are shown in the previous paragraph). The bicrystal parameters were determined by relevant documentation [53,54]. Microstructures such as the dislocations and deformation twins were characterized by FEI-G^{2}20 transmission electron microscope (TEM) with a 200 kV working voltage. The TEM specimens were prepared by electrolytic twin jet method with 5% perchloric acid + 95% absolute ethanol at 243 K.

2.4 Statistical methods of hydrogen-induced cracks

Digital image analysis technology was applied to perform for statistical analysis on the HICs. The specimen gauge after SSRT was manual suspension polished with a particle size of 0.04 μm to acquire high-quality SEM images of HICs. During this process, the thickness loss of the specimen is much less than 1 grain. First, the 2D HICs were extracted from the original SEM image through a color extraction algorithm [55], in which the target pixel was set to the red-green-blue value of black, the neighborhood was set to 3 and the tolerance was set to 10 (Fig. 2(a)). Then, the isolated noise pixels

were removed from the extracted image. Two sets of algorithms are needed to calculate the HICs length. To show the shape of the crack clearly, we enlarged the HICs in the green box in Fig. 2(a). However, in actual statistical analyses, all the HICs would be calculated over the entire area. The medial axis thinning algorithm was used to calculate the HIC length because the HICs are twisted and do not form regular straight lines (Fig. 2(b)). The medial axis has the same Euclidean distance from two boundaries between the HIC and the matrix which accurately describes the tortuous HIC length (Fig. 2(b1)). The medial axis of each HIC was calculated as shown in Fig. 2(b2). Then, considering that each HIC is not interconnected, the 8-connectivity algorithm was adopted to segment the extracted HICs skeletons and automatically count the total HIC numbers (Fig. 2(c1)). Diagonal HIC pixels are considered as members of the same group, which is consistent with the experimental facts. The segmented HIC skeletons are labeled to calculate the pixel length (Fig. 2(c2)). Then, based on the resolution, the pixels of each HIC length were converted to the physical length to obtain the length distribution and the total HIC number.

2.5 Determination of fractal dimension

The box counting algorithm was used to calculate the fractal dimension of the HICs and RGB. To avoid random errors caused by the selection, six subregions with a pixel size of 512 × 512 were selected on the extracted binary image in the size of 1024 × 768 pixels. Each subregion was covered with a grid with different box sizes (δ). Last, the total number Nt of boxes containing HICs pixels was counted (Fig. 3(a)). The

following power law was used to calculate the fractal dimension (D_f):

$$N_t(\geq \delta) = \delta^{-D_f}$$

The mean *Df* value of all subregions was regarded as the fractal dimension for an entire image. Fig. 3(c) shows the double logarithm of the box size (δ) and number (Nt) for HICs. For RGB images, the first step was to use the color extraction algorithm to extract the RGB distribution (Fig. 3(b)). Fig. 3(d) shows the double logarithmic of the box size (δ) and number (N_t) for RGBs. The detailed calculation process is recounted in our previous study [18]. Even though HIC and RGBs are both observed in SEM, HICs are obtained with a lower magnification, while RGBs are obtained with a higher magnification. So it's called "micro" and "macro" level in the following.

3. Results

3.1 Grain boundary microstructure characteristics

number (Nt) for RGBs. The detailed calculation process is recounted in our previous study [18]. Even though HIC and RGBs are both observed in SEM, HICs are obtained with a lower magnification, while RGBs are obtained with a higher magnification. So it's called "micro" and "macro" level in the following. Fig. 4 shows the GBCD maps, inverse pole figure (IPF) and (111) plane pole diagram. Different grain boundary types are represented by different colors (Σ3 (red), Σ9 (blue), Σ27 (green), other low-ΣCSL grain boundary (yellow), RGB (black)), as shown in Fig. 4(a1–d1). This finding shows that a large number of Σ3, Σ9 and Σ27 grain boundaries are clustered

together and they form many triple junctions, such as Σ3-Σ3-Σ9 and Σ3- Σ9-Σ27. In addition, we could observe a cluster of grains where each grain is connected to at least one other grain by a Σ3n (n = 1, 2, 3) boundary, so-called "grain clusters". The uniformly distributed austenite grains were found in all specimens shown for IPF (Fig. 4(a2–d2)). Fig. 4 (a3–d3) shows (111) plane pole figure of iso-density line distribution. The microtexture intensity is very weak (maximum: 1.6) judged from the density of iso-density lines, which shows that there is no microtexture in TWIP steels. Therefore, the effect of the microtexture on hydrogen-induced cracking was excluded. Table 2 shows the length fractions of different grain boundary types over the total grain boundary length (the value is an average of three EBSD scanning areas at least) and the average grain size (*d*ave) in these specimens. From the length fractions of the grain boundary, the fraction of Σ3n type grain boundaries ($F\Sigma$3n) is 10–50% in these specimens; the G1 has the highest $F\Sigma$3n (47.29%) and G3 has the lowest one (17.88%). For the Σ3 GB fraction ($F\Sigma$3), the highest $F\Sigma$3 is G1 (40.69%), while the lowest $F\Sigma$3 is of the G3 (15.69%); for the RGB fraction (*F*RGB), the highest *F*RGB is G3 (81.58%) and G1 has the lowest (51.45%). The grain boundary length fraction alone is insufficient to evaluate the efficiency of GBE. The RGB distribution in a grain boundary network should also be addressed [56]. In this study, the fractal dimension was applied to characterize the complex distribution of the entire RGBs network in each specimen quantitatively. The "complex " refers to the degree of irregularity or curvature, which is the so-called nonlinear system in mathematics. And the “irregularity” is relative to a regular geometric shape in the traditional Euclidean geometry. For the RGB,

it does not satisfy the regular shape in the Euclidean geometry and indifferent everywhere, so the dimension of Euclidean geometry cannot be used to quantitative characterize it. However, it can be quantitatively characterized by the fractal geometry, that is, to define a fractal dimension for irregular shape. The RGB fractal dimensions of all the specimens are follows: G1: 1.33, G2: 1.41, G3: 1.50 and G4: 1.34. This trend suggests that the larger the *F*RGB is, the larger the RGBs fractal dimension (in Section 4.2, the relationship between the fractal dimension of RGBs and HICs will be discussed). From the perspective of the average grain size (*dave*) considering both the grains and twins, there is no significant difference in the *dave* among these specimens; *dave* of the G4 is the largest (26.5 μm) and the G2 is the smallest one (21.8 μm). The difference between the largest grain size and the smallest is only within 5 μm.

3.2 Slow strain tensile test and fracture surface observation

Fig. 5(a) presents the engineering stress-strain curves for four specimens after SSRT in air. It shows that the ultimate tensile strength (UTS) of G2 and G4 specimens were almost equal (approximately 1104 MPa), and the value for the G1 was relatively lower (approximately 1055 MPa). The difference between the maximum and the minimum UTS value is less than 5%. Therefore, the four specimens can be used to compare the E_{loss}. Fig. 5(b–e) shows the engineering stress-strain curves at two strain rates (1×10^{-5} s^{-1} and 1×10^{-6} s^{-1}). The black curve in each figure represents that a specimen was subjected to SSRT in air. The blue and red curves show a specimen that was subjected to SSRT with in situ hydrogen-charging (blue: 1×10^{-5} s^{-1}, red: $1 \times 10^{-}$

6 s^{-1}). Fig. 5 (b–e) clearly shows that the plastic loss at a 1×10^{-6} s^{-1} is greater than that at a 1×10^{-5} s^{-1} for four specimens, i.e. the E_{loss} increases with the decreasing strain rate (Table 3). By combining Tables 2 and 3, the E_{loss} is shown to increase with the $F\Sigma 3$ decreases, regardless of the fact that a SSRT was conducted at 1×10^{-5} s^{-1} or 1×10^{-6} s^{-1}. And the relationship figure between E_{loss} and $F\Sigma 3$ is shown in the Fig. 5(f). The differentiation of this change trend is significantly obvious at a 1×10^{-5} s^{-1}, but it is not obvious at a 1×10^{-6} s^{-1}. Nevertheless, when comparing the two specimens with the largest and smallest $F\Sigma 3$ (G1: 47.29%, G3: 17.88%), there is still a 10% numerical difference in the E_{loss} (G1: 77.5%, G3: 87.6%). Therefore, we can be clearly concluded that the E_{loss} decreases as the $F\Sigma 3$ increases in TWIP steels. Since the G1 has the highest $F\Sigma 3$ and the corresponding E_{loss} is the smallest, the G3 shows the opposite trend. Hence, the characterization test to follow was primarily based on G1 and G3. Fig. 6(a, b) shows the XRD patterns of these specimens before and after SSRT in air, which indicates that TWIP steels can maintain their austenite phase stability. For the two specimens with the lowest and highest E_{loss} (G1 and G3), they did not undergo martensite transformation and could still maintain austenite stability before and after SSRT with hydrogen-charging Fig. 6(c, d). Fig. 7 presents the fracture morphology of G1 and G3 specimens after SSRT at two strain rates. Both specimens exhibit typical morphological character of high strength steels undergoing hydrogen embrittlement, i. e. the brittle fracture zone is around specimens (Fig. 7(a2–d2)) and the ductile fracture zone is in the center (Fig. 7(a3–d3)). The cleavage or quasi-cleavage morphological features were also observed on the brittle fracture zone of G1 with a 1×10^{-5} s^{-1} (Fig. 7(a2)), which corresponds to

the lowest E_{loss} in G1. However, at a 1 × 10^{-6} s^{-1}, the intergranular fracture character are more obvious. The ductile fracture zone is primarily dominated by dimple character, as shown in Fig. 7(a3, b3). However, for G3, whether at a 1 × 10^{-5} s^{-1} or 1 × 10^{-6} s^{-1}, the brittle fracture zone is an intergranular fracture (Fig. 7(c2, d2)) and the ductile fracture zones is a ductile dimple fracture (Fig. 7(c3, d3)), which corresponds to the highest E_{loss}. Furthermore, for G3 at a 1 × 10^{-6} s^{-1}, parallel traces appear on the facet in the intergranular zone, as shown by the green box in Fig. 7(d2) ((d4) is the enlarged image). The fraction of brittle area results relationship between *AB/T* and *FΣ3* was shown in Fig. 5(f) and Table 3. It can see that *AB/T* at a 1 × 10^{-6} s^{-1} strain rate is significantly greater than that at a 1 × 10^{-5} s^{-1} and also decreases with the *FΣ3* increase, which is consistent with the changing trend of E_{loss}.

3.3 Hydrogen-induced crack statistics

According to the calculation method in Section 2.4, the statistics addressed the HIC number and length for the G1 and G3 at a macro scale. The specimens (G1 and G3) were unloaded when the SSRT reached 10% strain at a 1 × 10^{-6} s□ 1 strain rate based on the red engineering stress-strain curve in Fig. 5(b, d). Then the HICs on a specimen surface were counted. Nevertheless, at a 1 × 10^{-5} s^{-1} strain rate, both specimens were unloaded when the SSRT was performed at 20% and 27% strain, respectively. Fig. 8 shows the statistical results. The statistical histogram, cumulative frequency curve, HIC numbers and average lengths are presented in each figure. The

statistical histogram represents the percentage of the total number of cracks in each length interval. The cumulative probability represents the cumulative frequency of each length interval percentage. The statistical results of the two specimens with a 1×10^{-6} s^{-1} strain rate is shown in Fig. 8(a, b). In terms of the number of HICs, G1 specimen has less HICs than G3 (G1: 97, G3: 118) and the average length of G1 is shorter than that of the G3 as well (G1: 14.5 μm, G3: 22.2 μm). From the statistical histogram, the length with approximately 10 μm percentage length is relatively higher in G1 (all above 15%), and the highest length percentage is 10 μm (23%). And HICs with a length of less than 20 μm account for 80% of the total number of cracks, and the average crack length of 14.5 μm is also distributed in this range. In contrast, the length (approximately 20 μm) percentage of the G3 is relatively higher (higher than 15%) and the crack percentage with 20 μm length is the highest (29%). This finding is roughly consistent with average crack length of 22.2 μm. Finally, from the cumulative frequency curve, the cumulative frequency reached 95% when the HIC length reached 30 μm in G1, which indicates that a few HICs are longer than 30 μm and the number is approximately 5. Of course, for HICs with a length of 50–60 μm, this may be the result of the shorter HICs coalescence [57,58]. By contrast, for the G3, the cracks length reaches 60 μm before the cumulative frequency reaches 95%, which is significantly longer than those of the G1. There are also a few long HICs in the G3 (the longest is 90 μm). Therefore, at a strain rate of 1×10^{-6} s^{-1}, the short HICs were used to study crack initiation, in other words, the HICs between two grains (the size is less than or equal to the average grain size) are regarded as the HICs initiation, but the long HICs were used to study

HICs propagation (see Section 3.4 for specific results). The HIC statistical results are shown in Fig. 8(c, d) for G1 and G3 specimens which were loaded to 20% strain at a 1 × 10^{-5} s^{-1}. Within the statistical area of the same size, the HIC number was 64 and the average crack length was 14.5 μm in G1, while for G3, the HICs number was 79 and the average crack length was 20.7 μm. By contrast, the number of HICs in G3 was larger and the average crack length was longer than that of G1. From the statistical histogram and the cumulative frequency curve, the HIC length is mainly distributed approximately 20 μm in G1, the cumulative frequency reached 80% and the increase rate was particularly fast. When the HIC length was 30 μm, the cumulative frequency reached 98% (Fig. 8(c)). For cracks with a length of greater than 30 μm, the cumulative frequency increases slowly. The length of HICs in G3 has no obvious concentration distribution range and the cumulative frequency was continuously increasing (Fig. 8(d)). When the HICs length was 35 μm, the cumulative frequency reached 80%. When the length is 45 μm, the increase in the cumulative frequency was relatively slow, but it still displayed a monotonous increase. This finding indicates that the HIC length distribution in G3 is wider than that of G1. Similarly, the 70% HICs percentage length was less than 25 μm for both specimens from the histogram of the crack length distribution. The length of most HICs is approximately equal to the grain boundary length between the two grains according to the average grain size of the specimens in Table 2 (G1: 23.6 μm, G3: 25.2 μm). Therefore, the HIC in which the specimens were tensile until 20% strain at a 1 × 10^{-5} s^{-1} strain rate was used to investigate the crack initiation. In addition, the statistical histogram in Fig. 8(c, d) shows double peaks. the second small peak

appears at about 30 μm (G1) and 40 μm (G3). We can infer that a small part of the crack propagated but did not coalesce a longer crack at 20% strain according to the average grain size of the two specimens (G1: 23.6 μm, G3: 25.2 μm). Fig. 8(e, f) shows the HICs statistical results when the SSRT reached 27% strain at a 1×10^{-5} s^{-1} strain rate. The number of HICs, G1 has less HICs than G3 (G1: 127, G3: 151). From the average crack length, the G3 is 31.8 μm, which is significantly longer than G1 (21.6 μm). Fig. 8(e) shows that the HIC length distribution is primarily concentrated at 15–30 μm in G1 (the cumulative frequency is greater than 80%). However, the HIC length distribution is primarily concentrated between 20 and 45 μm in G3 (the accumulative frequency is greater than 80%, as shown in Fig. 8(f)), which is clearly longer than G1. Additionally, there are some HICs with a length greater than 100 μm in the two specimens. These HICs have multiple grain boundaries involved according to the average grain size. Therefore, the HICs in which specimens were tensile until 27% strain at a 1×10^{-5} s^{-1} were used to investigate the crack propagation. At the macro scale, Fig. 2(c2) indicates that the individual HIC distribution is irregular and thus the overall HICs distribution is also irregular in a certain area in addition to the quantity length on the specimen surface. According to the calculation method in Section 2.5, the fractal dimension was applied to characterize the HIC distribution at macro scale quantitatively. It is not appropriate to just compare the G1 and G3. Therefore, the complex HIC distributions of all four specimens were quantitatively characterized. For the small to large *Eloss* of the four specimens, the fractal dimension of the HIC (*D*HIC) under 27% strain was G1 → G4 → G2 → G3: 0.942 → 0.981 → 1.029 → 1.137, the

standard deviation as shown in Table 4. In combining the Tables 3 and 4, it is clear that as the *Eloss* increases, the *D*HIC also increases, i.e. the greater the *Eloss* is. However, taking into account that the *Eloss* evaluation in this work is based on the fracture strain, the *D*HIC of four specimens at fracture strain (G1: 40% strain, G2: 31% strain, G3: 27% strain, G4: 33% strain) was calculated, the results are also shown in Table 4. For the small to large *Eloss* of the four specimens, the *D*HIC was G3 → G2 → G4 → G1: 1.137 → 1.171 → 1.209 → 1.228 (the standard deviation as shown in Table 4), which can be seen that under the fracture strain, the *D*HIC decreases with the *Eloss* increase. Under different strains, the specific reasons for the different trends of the *D*HIC changing with *Eloss* will be discussed in Section 4.2.

3.4 EBSD observation and slip transfer analysis of HICs

3.4.1 Hydrogen-induced cracks initiation

Fig. 9 presents the SEM and EBSD images of HICs initiation for G1 and G3 specimens at two strain rates. In this study, the HICs between two grains (the size is less than or equal to average grain size) are regarded as the HICs initiation. The HICs initiation map of the two specimens at a 1×10^{-6} s^{-1} strain rate is shown in Fig. 9(a, b). Clearly, all the HICs initiated at the grain boundaries. The grain on the right side of the HIC clearly showed band-like morphologies in G1 (Fig. 9(a1)). With identification by the IPF (Fig. 9(a2)), these bands are slip bands formed by dislocations planar slip. Regarding how to distinguish these bands within the grains formed during SSRT at different strain rates in TWIP steels, the slip bands were easier to form by dislocation

slip at a 1 × 10□ 6 s□ 1 strain rate studied in our previous study [7]. For G3, there are no slip bands within the grains (Fig. 9(b1)) (the reason will be discussed in Section 4.1). Nonetheless, the grain boundaries where HICs occurred are also RGB, as shown in Fig. 9(b2). The HIC initiation maps of both specimens at a 1 × 10□ 5 s□ 1 strain rate are shown in Fig. 9(c, d). There is an HIC parallel to the tensile direction in G1 (Fig. 9(c)). Here we need to clarify that most HICs on the G1 are approximately perpendicular to the tensile direction, but some HICs are parallel to the tensile direction as well. Interestingly, these HICs were not present in the G3 specimen (statistical results are shown in Fig. S2 in Supplementary material). There are a large number of bands within the grains on the upper and lower sides of the HIC as well (Fig. 9 (c1)); these bands are deformation twins combined with the IPF, as shown in Fig. 9(c2) (the specific identification method was introduced in detail in our previous study [7]). The left part of this HIC is on the grain boundary (the grain boundary is RGB), and the right part is within the grain. At the same time, there is a grain boundary perpendicular to the tensile direction but no crack occurred, and the grain boundary is a $\Sigma 3$ grain boundary based on the IPF (Fig. 9(c2)). For G3, all HICs are approximately perpendicular to the tensile direction, as shown in Fig. 9 (d). There are some bands within the grains on both sides of the HIC as well. Those bands are deformed twins and the grain boundary is RGB according to the IPF (Fig. 9(d2)).

3.4.2 Slip transfer analysis

Generally, for polycrystalline materials such as TWIP steels, the grains with

different orientations have different capacities for dislocation slip or deformation twining. Therefore, this phenomenon affects the homogeneous deformation ability at a micro level, which is determined by whether the slip transfer across a grain boundary. Regarding the evaluation method of the slip transfer within an adjacent grain, Luster–Morris [59] proposed a model for a geometric compatibility factor (m') based on the estimation of the alignment between two slip systems to quantify the slip transfer grain boundary cases. The specific schematic diagram of the bicrystal model is shown in Fig. 10. In this model, φ is the angle of the slip direction included within both adjacent grains ($\varphi = \cos^{-1}|\boldsymbol{d}_{in} \cdot \boldsymbol{d}_{out}|$), and θ is the angle of the normal of slip plane included within both grains ($\theta = \cos^{-1}|\boldsymbol{n}_{in} \cdot \boldsymbol{n}_{out}|$). The m' is defined as:

$$m' = \cos\theta \cdot \cos\varphi$$

The m' value range is 0–1. If the slip plane and slip direction of two adjacent grains are perpendicular, then $m' = 0$, which indicates that a slip cannot transfer across a grain boundary. If a slip plane and slip direction are parallel, then $m' = 1$, which indicates that the slip can completely transfer across a grain boundary. When the value of m' is between 0 and 1, a slip could partially transfer across a grain boundary and will leave residual dislocations on the grain boundary. Since the formation mechanism of deformation twining is similar to the dislocation slip process [60,61], there are specific crystal planes and directions, so this model is also applicable to deformation twining. The cubes were used to show the location of the unit cells within both adjacent grains on a side of those HICs and the slip or twining system within grains, as shown in each

SEM image (Fig. 9). In this study, the direction parallel to the tensile direction is assumed to be the tensile stress direction of each grain, and a slip or twin system of the maximum critical shear stress was determined as the active slip system. At a 1×10^{-6} s^{-1} strain rate, the bands within grains are slip bands. For G1, the activated slip system is $(1\bar{1}\,\bar{1})$ [101]within the right-side grain, and the left-side is (111)[$\bar{1}$10]. The m' value of the cracked grain boundary was 0.89, as shown in Fig. 9(a1). For G3, the activated slip systems are $(\bar{1}\,1\,\bar{1})$ [110] (left grain) and $(1\bar{1}\,\bar{1})$ [101] (right grain) within both adjacent grains, and the m' value is 0.89, as shown in Fig. 9(b1). At a 1 × 10□ 5 s□ 1 strain rate, the bands are deformation twins within these grains. For G1, the activated deformation twin systems were $(\bar{1}\,\bar{1}\,1)$ [2$\bar{1}$ 1] (upper grain) and $(\bar{1}\,1\,\bar{1})$ [2$\bar{1}$ 1] (lower grains) within the adjacent grains, and the m' value was 0.87 (Fig. 9(c1)). For G3, the activated deformation twin systems were $(\bar{1}\,1\,\bar{1})$ [121] (left grain) and $(\bar{1}\,\bar{1}\,1)$[$\bar{1}$ 2$\bar{1}$] (right grain) within both adjacent grains, and m' value was 0.84, as shown in Fig. 9(d1). The m' value distribution at these four cracked grain boundaries ranges from 0.84 to 0.89, which indicates that the dislocation slip or deformation twining could not completely transfer across the grain boundaries. Simultaneously, the value of m' is 1.00 at a Σ3 grain boundary that is perpendicular to the tensile direction, but this grain boundary did not crack and the activated deformation twin system is $(\bar{1}\,\bar{1}\,1)$[$\bar{1}\,\bar{1}\,\bar{2}$] on the right side, which indicates that the deformation twining can completely transfer across this grain boundary (Fig. 9(c1)). Similarly, the m' value of the non-cracked grain boundary and the activated deformation twining system were calculated at a 1×10^{-5} s^{-1} strain rate, as shown in Fig. 11. These grain boundaries are all approximately

perpendicular to the tensile direction, and there are some deformation twins or slip bands within both grains. The m' values are 0.94 (Fig. 11(a1)) and 0.99 (Fig. 11(b1)), and these two grain boundaries are RGB (Fig. 11(a2)) and $\Sigma 3$ grain boundary (Fig. 11(b2)). The m' values range from 0.94 to 1.00 of the three non-cracked grain boundaries in Figs. 9(c) and 11. Therefore, the m' value of the cracked grain boundary is smaller than that of the non-cracked grain boundary. In addition to the geometric compatibility parameter (m'), the difficulty of a slip transfer on a grain boundary also depends on the minimum residual Burgers vector (br) of dislocations remaining on a grain boundary. Based on the method of Lee et al. [62,63], br is defined as:

$$b_r = |\boldsymbol{b}_{in} - \boldsymbol{b}_{out}|$$

where $\boldsymbol{b}in$ and $\boldsymbol{b}out$ are the Burgers vectors of a dislocation slip into and out of a grain boundary, respectively. The results of the calculation are marked in the SEM images of Figs. 9 and 11. For the four cracked grain boundaries, the br value is between 0.21 and 0.30 (Fig. 9(a1–d1)). For the three non-cracked grain boundaries, the br value is between 0.02 and 0.15 (Figs. 9(c1) and 11). Clearly, the br at the cracked grain boundary is larger than the br at non-cracked grain boundary.

3.4.3 EBSD observation of hydrogen-induced crack propagation

Fig. 12 shows the SEM and EBSD images of HICs propagation for G1 and G3 at two strain rates. The slip traces were marked pink and black dotted lines within an adjacent grain on both sides of the HIC, i.e. {111} plane traces (Fig. 12(a1–d1)). The cubes were used to mark a crystal cell orientation within grains in IPF (Fig. 12(a2–d2)),

and each color line represented a grain boundary in the Fig. 12(a3–d3). The color lines were consistent with Fig. 4(a1–d1). At a 1 × 10-6 s-1 strain rate, the HIC propagation paths are approximately parallel to the direction of the {111} plane trace, as shown in Fig. 12(a1, b1), and all the HICs propagate along grain boundaries (Fig. 12(a2, b2)). In addition, there is a Σ3 grain boundary at a HIC tip or deflection, as indicated by the blue arrows in Fig. 12(a3, b3). At a 1 × 10-5 s-1 strain rate, the HIC propagation paths are approximately parallel to the direction of the {111} plane trace (Fig. 12(c1, d2)), and HIC propagate along grain boundaries as well (Fig. 12(c2, d2)). There are also Σ3 grain boundaries at the tip and the HIC deflection position (Fig. 12(c3, d3)). This result also shows that a Σ3 grain boundary hinders HIC propagation. Additionally, there are other low-ΣCSL and Σ27 (Σ3n, n = 3) grain boundaries in a HIC propagation paths, as indicated by the green arrow in Fig. 12(c3).

3.5 TEM observation of dislocation configuration on the grain boundary

Fig. 13 shows the TEM image of dislocations configuration at a grain boundary when the G1 and G3 were deformed to the 10% strain at a 1 × 10□ 6 s□ 1 strain rate with hydrogen-charging. The dislocation character was observed at different types of grain boundaries by ***g***-vector analysis. A Σ3 grain boundary was determined by selection area diffraction under the <110> crystal axis (Fig. 13(a1)). Under $\boldsymbol{g}=\bar{1}\,\bar{1}1$, the stacking faults (Fig. 13(a2) blue arrows) and some dislocations (Fig. 13(a2) green arrows) can be observed near or on this grain boundary. Under ***g*** = 02□ 2, all the

stacking faults and dislocations disappear, as indicated by the blue and green dotted arrows in Fig. 13 (a3).

Under $\boldsymbol{g}=\bar{2}00$, the stacking faults and dislocations reappeared near the grain boundary (blue and green arrows Fig. 13(a4)). These findings determined a Shockley partial dislocation with a $\frac{a}{6}\left[11\bar{2}\right]$ Burgers vector near the grain boundary and perfect dislocation with $\frac{a}{2}\left[01\bar{1}\right]$ Burgers vector on the grain boundary. Using the same method, a RGB with a *Misorientation* of 40.9 ° in the G3 specimen was determined under the <110> crystal axis, as shown in Fig. 13 (b_1). Under $\boldsymbol{g}=\bar{1}1\bar{1}$, there were many dislocations at this grain boundary, as indicated by the green arrows in Fig. 13(b2). Under $\boldsymbol{g}=\bar{2}00$, there were some dislocations did not disappear on the grain boundary (green dotted arrows in Fig. 13(b3)). For $\boldsymbol{g}=0\bar{2}2$, there were more dislocations on the grain boundary (the green arrows in Fig. 13(b4)). These dislocations could determine the Frank partial dislocation with a $\frac{a}{3}[11\bar{1}]$ Burgers vector near the grain boundary and perfect dislocation with $\frac{a}{2}[01\bar{1}]$ Burgers vector on the grain boundary. Fig. 14 shows the dislocation configuration near a grain boundary when the G1 and G3 with hydrogen-free were deformed to 10% at a 1 × 10□ 6 s□ 1strain rate. A Σ3 grain boundary is determined under the <110> crystal axis based on the selected area diffraction, as shown in Fig. 14(a). There are clear dislocation lines inside a grain, but a large amount of slip bands similar to those indicated by the red arrows in Fig. 13(a) were not observed. At the same time, there is no obvious dislocations pile-up near the grain boundary. Fig. 14(b) shows thedislocation configuration near a RGB. There are

higher density dislocation walls or cells inside the grains, but the slip bands similar to those indicated by the red arrows in Fig. 13(b) are not clearly observed as well. There are no slip bands that intersect with a grain boundary in these two TEM images. It should be noted that the dislocations configuration character is not individual phenomenon. In the experiment, we have observed many areas with similar results. Previous Gutierrez-Urrutia I et al. [64] also reported that there are only high-density dislocation regions in TWIP steel at lower strain in air, but no slip bands. We know that hydrogen can promote the movement of dislocations and reduce the stacking fault energy of austenite [65], hindering the occurrence of dislocations cross-slip and making dislocations planar slip more likely to eventually form a slip band.

4. Discussion

4.1 Effect of slip transfer on HICs initiation

Hydrogen-induced cracking is known to be the result of the coupling of hydrogen and stress when metal materials undergo microstructural evolution under stress. In other words, HIC initiation is related to the microstructure character and mechanical (stress or strain) at the micro level. Therefore, in this section, the HICs initiation was explored and the general law was sought from a statistical perspective as well. The interaction of the dislocation planar slip and deformation twins with grain boundaries plays an important role in the HICs initiation, which has been reported in our previous studies for TWIP/TRIP steels [7]. In addition, Koyama and Park et al. [6,33] found that the stress concentration generated by the interaction between the deformed twins and the

grain boundaries would promote the HIC initiation. In this study, a similar phenomenon was observed in Fig. 9. It seems that the slip bands or deformation twins were a "*killer*" that caused the HIC initiation in TWIP steels. However, as shown in Fig. 11, even though there were interactions between the deformation twins and grain boundaries within both grains (the grain boundaries are almost perpendicular to the tension direction), hydrogen-induced intergranular cracking did not occur. This result indicates that the dislocation planar slip or deformation twining was a necessary conditions for HIC initiation. To engineering structural materials using polycrystalline metal with austenite structures such as TWIP steels, the heterogeneous deformation depends on the local microstructure evolution. In addition, the degree of grain deformation is different due to the different crystal orientations under the deformation constraint within adjacent grains. Deformation near the grain boundaries could mediate the strain jump, which indicates that the grain boundaries may serve as a strong barrier to dislocation slip or deformation twining. Dislocation slips or deformation twining either stop at a grain boundary to produce geometrically necessary dislocations (GNDs) or they are easily slipped in transfer across the grain boundary to an adjacent grain, in other words, new dislocations would generate in adjacent grains due to the activation stress concentration at the grain boundary, so the stress or strain can be relaxed at the grain boundary, leading to deformation on a different slip or twin systems in an adjacent grain. Generally, the prerequisite for the occurrence of slip transfer grain boundary is that a slip system within an adjacent grain needs to be activated for slip deformation. The activated slip system within a grain depends on the Schmid factor. The larger the Schmid factor, the

softer the grain orientation, and the more easily activated the slip system. From this, the Schmid factor of an adjacent grain can be calculated. It is well known that the most intuitive feature of an activated slip system is the formation slip band. At a 1×10^{-6} s^{-1} strain rate, the clear slip bands were only shown in the grain on the right side of HIC in G1 (Fig. 9(a1)), but no clear slip bands appeared in the other three grains (Fig. 9(a1, b1)). According to the calculation results of the Schmid factor, the values are 0.478 (left) and 0.480 (right) on both sides of the HIC in G1 and are 0.466 (left) and 0.468 (right) in G3. Therefore, the Schmid factor could provide information whether the slip deformation tendency or easiness within a grain. Based on the analysis results in 3.4.2 (Figs. 9 and 11), it's clear that the m' value for the non-cracked grain boundaries is significantly larger than that of the cracked grain boundaries. This finding indicates that these slip or deformation twining are more likely to transfer across a non-cracked grain boundary, but a cracked grain boundary has a strong hindrance to slip or deformation twining. Moreover, the cracked grain boundaries are all RGBs. Interestingly, even the RGB did not crack in this study, as shown in Fig. 11(a). From the perspective of the m' value, the m' value of this RGB is 0.94, which is significantly larger than that of a cracked grain boundary (Fig. 9). In other words, if slip or deformation twining could transfer across the grain boundary to a large extent, even RGBs crack will not crack. It is well known that the *Misorientation* of different RGBs is different [66,67]. Compared to the *Misorientation* of a cracked RGB, the *Misorientation* of a non-cracked RGB was indeed different. The *Misorientation* distribution range is 27.4–45.1◦ for four cracked grain boundaries (Fig. 9(a2–d2)), and

the *Misorientation* of three non-cracked grain boundaries is 21–59.6◦ (Fig. 9(c2) and 11(a2)). From the perspective of the *Misorientation* alone, no change law has been found. The reason may be due to the small number of cracked or no-cracked grain boundaries. In addition, regardless of the cracked or non-cracked grain boundary, the m' values of these grain boundaries had a range of 0–1.00, as shown in Figs. 9 and 11. This finding shows that the slip or deformation twining could not transfer completely across these grain boundaries into an adjacent grain, which can be certain that there same GNDs on a grain boundary. Meanwhile, there must be a certain *br* for the residual dislocations. From the calculation results of *br* in Section 3.4.2, the *br* of a cracked grain boundary were larger and non-cracked grain boundaries. In short, the cracked grain boundaries have a stronger hindrance to slip or deformation twining transfer, i.e. their m' value is smaller than that of these non-cracked grain boundaries and *br* value is greater. Nonetheless, the discussion in the above paragraph is limited to the seven grain boundaries as shown in Figs. 9 and 11, and the rule of hydrogen-induced intergranular cracking is not statistically significant. Therefore, a statistical analysis was performed for the m' , *br*, and *Misorientation* of cracked grain boundaries and non-cracked grain boundaries. Among them, 67 grain boundaries (134 grains) were cracked, and 64 grain boundaries (128 grains) were not cracked. In the statistical analysis, the ability to activate the slip or deformation twining system was first ensured for each grain. Only in this way can the slip or deformation twining transfer across grain boundaries possibly occur in both adjacent grains. Therefore, the Schmid factor of all the grains should meet the minimum value required to activate the slip or twining

system. It is important to note that all the grain boundaries we counted are in a perpendicular or approximately perpendicular relationship with the tension direction. Fig. 15 shows the IPF for cracked and non-cracked grains, which also shows the grain orientation and Schmid factor for, respectively. The Schmid factors are all greater than 0.33, which can be used to investigate the slip or twining transfer across grain boundaries [68]. Additionally, there is no particularly obvious preferred micro crystal orientation for the cracked or non-cracked grains. Fig. 16 summarizes the *Misorientation*, *br* and *m′* of the statistics for 131 grain boundaries. From the statistical results (Fig. 16(a, c)), the *Misorientation* distribution of the cracked grain boundaries is 25–53◦, but those from 38◦ to 50◦ are the most concentrated; the range of *Misorientation* distribution for non-cracked grain boundaries was found to be 20–60◦, but there were non-cracked grain boundaries distributed from 40◦ to 47◦. It is more obvious that the *m′* value of a cracked grain boundary is less than 0.93 (0.71–0.93), while the *m′* value of a non-cracked grain boundary is greater than 0.93 (0.93–1), as shown in Fig. 16(a, b). For *br* value, the *br* values of these cracked grain boundaries are all greater than 0.19 (0.19–0.34), and the *br* values of these non-cracked grain boundaries are less than 0.19 (0–0.19) (Fig. 16(b, c)). It is worth noting that the data points circled by green dotted lines in Fig. 16(a–c) correspond to Σ3 grain boundaries, which can be seen that the *m′* value are approximately equal to 1 and the *br* value are less than 0.15. It can be determined that slip or deformation twining could slip transfer Σ3 grain boundary. The regions where imitation (red) and non-imitation grain boundaries (green) are shown in the *Misorientation*, *br* and *m′* three-dimensional

diagrams (Fig. 16(d)). From the above statistical results, the critical value of the cracked grain boundary is $m' < 0.93$, $br > 0.19$. This can be concluded that when the grain boundaries served as a large hindrance to a slip or deformation twining transfer, more dislocations could pile up at grain boundaries and the *br* of these dislocations are relatively large. According to hydrogen-enhanced localized plasticity (HELP) theory [69–72], hydrogen can promote dislocation movement. In addition, hydrogen could also reduce the stacking fault energy in austenite materials [65]. In this way, dislocations are more prone to planar slip and then form slip bands. This phenomenon has been observed under TEM (Figs. 13 and 14). As the dislocation slips toward the grain boundary, the dislocation would carryhydrogen atoms to the grain boundaries. Few dislocations could slip transfer across the grain boundaries within adjacent grains, and more dislocations could remain on grain boundaries. The dislocations that slipped across the grain boundary were not enough to carry these hydrogen atoms away from grain boundaries. As a result, more hydrogen atoms remain on grain boundary and less was carried away. Thus, excess hydrogen atoms appear on a grain boundary. Furthermore, a strain concentration could be caused due to the existence of GND stress fields piling up at the grain boundaries. And the larger *br* will cause a certain degree of grain boundary deformation [73], which generates strain concentration near the grain boundary. Combined with the TEM analysis in Section 3.5 and the lattice parameter of TWIP steels (a = 0.351 nm), $a6[2\square\ 11]$ = 0.14 nm can be calculated on a $\Sigma 3$ grain boundary. However, there are Frank partial dislocations with a $a3[111\square\ ]$ Burgers vector and some perfect dislocations with a $a2[011\square\ ]$ Burgers vector on a RGB (Fig.

13(b2–b4)). Frank partial dislocations' Burgers vector is larger than that of Shockley (i.e. $a3[111\square] = 0.21\text{nm} > a6[2\square 11] = 0.14\text{nm}$ and $a2[011\square] = 0.25\text{nm} > a6[2\square 11] = 0.14\text{nm}$). This further indicates that the Burgers vector of dislocations near $\Sigma 3$ grain boundary is smaller than that near RGB. This also means that a dislocation with a large Burgers vector will produce a large strain concentration on a grain boundary. Under the induction of the stress and strain field, hydrogen atoms would diffuse towards the grain boundaries, which could enrich more hydrogen atoms on the grain boundaries. According to hydrogen-enhanced decohesion (HEDE) theory [74–76], hydrogen could reduce the force between the atomic bonds of metal matrix. The hydrogen atoms that were enriched in a grain boundary would reduce the bonds force between the atoms at the grain boundary. This reduction would initiate HICs under an applied load, as shown in Fig. 17(a). When a grain boundary has little hindrance towards slip or deformation twining transfer (even without any obstacles), there are few dislocations remain on a grain boundary, and the *br* is also small. At that time, the hydrogen atoms carried by a slip-in dislocations to the grain boundary are mostly (even completely) transported into the lattice of adjacent grains by a slip-out dislocation due to the binding energy between the dislocations, grain boundaries and interstitial positions and hydrogen are roughly equivalent (26–35 kJ/mol) [77,78]. In addition, the stress and strain concentration caused by the dislocations remaining on the grain boundaries is also small, which is not enough to induce more hydrogen atoms to diffuse to the grain boundary, so it is not easy to initiate hydrogen-induced intergranular crack, as shown in Fig. 17(b). The *Misorientation is usually* related to grain boundary type. Among these cracked grain

boundaries, other low-ΣCSL (except Σ3n, n = 1, 2 and 3) grain boundaries accounted for 5% and RGBs accounted for 95%, but no cracked occurred at a Σ3 grain boundary, as shown in Fig. 18(a). *Misorientation* close to 60◦ gathers some data points in Fig. 16(a, c) and these data correspond to the Σ3 grain boundaries. More importantly, the m' value of these grain boundaries is close to 1.00, and the *br* value is very small (< 0.15). This result shows that the slip or deformation twining can transfer across to a Σ3 grain boundaries into an adjacent grain. Even if the slip or deformation twining are not fully transferred across, the *br* is also small. This finding shows that Σ3 grain boundary has weak resistance to dislocation slip and deformation twining. By contrast, the data points with a *Misorientation* of 40–48◦, correspond to cracked RGBs ($m' < 0.93$, $br > 0.19$). This observation further illustrates that it is relatively difficult for slip or deformation twining to transfer across a RGB. In combining the above discussion and statistical analysis, the response of a grain boundary to slip or deformation twins within an adjacent grain plays an important role in HICs initiation, which could be affirmed for TWIP steels during a SSRT. If a grain boundary has a large hindrance to slip or deformation twining transfer ($m' < 0.93$), more GNDs must be left on this grain boundary during the slip transfer process and the *br* is large as well. In this way, the stress or strain concentration will appear on the grain boundary. Hydrogen will diffuse to the grain boundary under the stress or strain induction, and eventually lead to HIC initiation. Thus, RGBs ($m' < 0.93$ and $br > 0.19$) parallel to the tensile direction could also initiate HICs ($m' = 0.82$, $br = 0.21$ in Fig. 9(c)). We know that once HIC initiate, there is a tendency to propagate. The transverse HIC have propagated into a grain under

the effect of a three-dimensional stress at the crack tip in Fig. 9(c). This effect causes the occurrence of a partial transgranular HIC, which corresponds to the fracture character of cleavage or quasi-cleavage in the brittle zone of the fracture surface (Fig. 7(a2)).

4.2 Effect of grain boundary character on HICs propagation

As previous Section 3.4, the HICs almost propagated along grain boundaries. Therefore, HICs propagation could have a specific relationship with the grain boundary type at a micro level. The HICs propagate along RGBs (Fig. 12) and other low-ΣCSL grain boundaries (except the Σ3n grain boundaries at n = 1, 2 and 3) also appeared on a crack propagation paths, as shown with green arrows in Fig. 12(b3 and c3). More notably, there are Σ3 grain boundaries distributed at a crack tip, as indicated by blue arrows in Fig. 12(a3 and b3), and the HICs experienced deflection when they encountered a Σ3 grain boundary in the most favorable direction for crack propagation. According to fracture theory [79], HICs are more likely to propagate in a direction perpendicular to the tensile direction. The position of a Σ3 grain boundary (marked by the blue arrows in Fig. 12(a3 and b3)) was in the most favorable position for cracks propagation, but the crack turned to the adjacent RGB to propagate. This result indicates that a Σ3 grain boundary hinders HIC propagation. Of course, this phenomenon is not limited to the four HICs shown in Fig. 12, so the statistical analyses were conducted on 120 HICs to explore the general low in the grain boundary character role in HIC propagation. The statistical results are shown in Fig. 18. Fig. 18(a) shows the fraction

of HICs propagated along different grain boundary types in 120 HICs, Fig. 18(b) presents the normalized cracked fraction of each grain boundary type. The probability of HIC propagation along RGBs is 75% (normalized cracked fraction is 24%), the probability of other low-ΣCSL grain boundaries (except Σ3n type grain boundaries n = 1, 2 and 3) is 23% (normalized cracked fraction is 9%). The probability of HICs to propagate along Σ3n grain boundaries is 2% (normalized cracked fraction is 0.4%). Therefore, it can be concluded that HICs propagate along RGBs, there is a possibility of propagating along other low-ΣCSL grain boundaries. The Σ3n grain boundary hinders the HIC propagation in TWIP steels. For RGB, the arrangement of atoms on grain boundaries is usually chaotic [11,80] and grain boundary energy is relatively high [81]. The dislocations would be more likely to pile up at RGBs during a SSRT, which will lead to an increase in the elastic strain energy at the grain boundaries, so RGBs more easily provide a convenient path for HIC propagation. The other low-ΣCSL grain boundaries were forced to crack under the action of three-dimensional stress at a crack tip when a HIC encountered other low-ΣCSL grain boundaries. In the Section 4.1, we confirmed that the m' values are relatively small (< 0.93) and the br is large (> 0.19) for the grain boundaries with *Misorientation* of 40–48◦, which shows that these grain boundaries have a greater hindrance to slip or deformation twining and elastic strain energy will also be generated on the grain boundaries as the more GNDs are likely to pile up at those grain boundaries, so grain boundaries stability could be decreased. Therefore, HICs can also propagate along other low-ΣCSL grain boundaries. For Σ27 (Σ3n, n = 3) grain boundary, even though Σ27 grain boundary is a secondary variation

of $\Sigma 3$ grain boundary, the energy of the grain boundary is also higher than that of $\Sigma 3$ grain boundary due to the small number of coincident lattices on grain boundary [82]. Also, the *Misorientation* of a $\Sigma 27$ grain boundary is 31.5◦ or 35.4◦, for which the corresponding value of m' is also relatively large [83]. According to the statistical results of cracks initiation (Fig. 18(a)), the probability of HIC initiation at $\Sigma 27$ grain boundary is 0%, so the $\Sigma 27$ grain boundary is also forced to crack during HICs propagation. A $\Sigma 3$ grain boundary hinders HIC propagation because its structure is stable and the grain boundary energy is low compare to RGB. Furthermore, in this study, the slip and deformation twining could slip transfer across a $\Sigma 3$ grain boundary ($m' \approx 1$), so it is not easy to produce stress or strain concentration on a $\Sigma 3$ grain boundary caused by GNDs. Therefore, the higher the *FΣ3* is in TWIP steels, the stronger the resistance of the steel to hydrogen-induced cracking. From the specific *Eloss* data (Table 3), no matter at a 1×10^{-5} s□ 1 or 1×10^{-6} s^{-1} strain rate, the *Eloss* of G3 specimen is higher than that of G1. However, at a 1 × 10□ 5 s□ 1 strain rate, G1 has the lowest *Eloss* (50.6%), while G3 has the highest *Eloss* (70.1%), and the difference between the two is close to 20%. At a 1×10^{-6} s^{-1} strain rate, this change trend is not particularly obvious. The influence of *F*Σ3 on *Eloss* became weak with strain rate decreases. As we know, reducing the strain rate directly affects the SSRT duration. In this study, the SSRT duration is about 8 h at a 1×10^{-5} s^{-1} strain rate, but at a 1×10^{-6} s^{-1} strain rate, the SSRT duration is about 46 h (G1). In this way, under the same hydrogen charging current, more hydrogen will enter the specimen at a low strain rate. Therefore, this indicates that hydrogen has a stronger ability to promote local plastic

deformation, which in turn is more likely to cause greater localization of stress or strain and more likely to form a main crack to cause final fracture. Therefore, the effect of $F\Sigma3$ on *Eloss* is weakened at a lower strain rate**.** Additionally, other researchers' work has shown that there is a phenomenon of hydrogen-induced twin separation in austenitic stainless steel (flat facets appear in the cleavage or quasi-cleavage area on the fracture surface), that is, the twin boundary ({111} $\Sigma3$ grain boundary) acted as a crack initiation position [84,85]. However, this phenomenon has not been found in this research work. The reason may be as follow: from the perspective of environmental factors, the hydrogen charging methods adopted by other researchers are pre-charge hydrogen with gas, resulting in relatively little hydrogen entering the material. So the fracture surface is usually characterized by cleavage or quasi-cleavage [86,87]. In this study, in-situ electrochemical hydrogen charging was used during a SSRT, hydrogen will continuously diffuse from the specimen surface to the inside, which could cause intergranular fracture under a low stress (Fig. 7(d2)). We know that the ability of hydrogen to diffuse inside the austenite lattice is significantly weak and annealing twins usually grow inside the austenite grains, so hydrogen is difficult to concentrate on the annealing twin boundaries. This indicates that hydrogen will preferentially weaken the grain boundaries rather than twin boundaries, which could promote intergranular crack initiate. For GBE, simply increasing the number density of special boundaries is insufficient to impact material properties related to grain boundaries in GBE field. Instead, it is the proper understanding of the distribution of such boundaries in the microstructure, which are of great significance. More precisely, the complexity of the

RGB network also needs to be modification and characterization that is responsible for the property improvement [56]. For the RGBs distribution complexity, the fractal dimension provided a precise mathematical method to quantitative characterize RGB network. It can be observed in Section 3.1 that the higher the *F*RGB is in TWIP steels, the more complex the RGB distribution. As can be seen from Table 4, the macro fractal dimension of HICs increases (under same strain: 27%) with the increasing *Eloss*. One point of particular note is the comparison of the relationship between *D*HIC and *Eloss* is performed after the specimens are deformed to the same strain (27%) at a 1×10^{-5} s^{-1} strain rate. We know that under the same strain (27%), the work done by the applied load on a specimen is the same, but the number of HICs on the G1 specimen is less than that of the G3 according to the HICs statistical results (Fig. 8(e, f)). At the same time, it can be seen from the statistical histogram that the length of HICs on G1 is mainly distributed around 20 μm (the average length is 21.6 μm), while the average grain size in G1 is 23.6 μm, which indicates that the large part of the crack path is only confined between two grains (Fig. 9). We know that the grain boundary in austenitic steels is relatively straight (small bending degree) from the morphology, so this leads to the smaller *D*HIC for G1 under 27% strain. Compared with G3, it has more and longer HICs (the average crack length is 31.8 μm), which indicates that most of the cracks have propagated. According to the average grain size (25.2 μm), it can be seen that a partial crack propagation paths involve at least two grain boundaries. Therefore, from the perspective of the crack morphology, the bending degree of HIC is greater, so the *D*HIC of will be larger. From the perspective of energy absorption, 27% strain is

close to the fracture strain for G3, and it is impossible to increase external energy. But for G1, only continuous application energy can make its HICs which paths limited to the between the two grains continue to propagate. Therefore, under the same strain (27% strain), the smaller the *D*HIC, the lower the *Eloss*. However, under the fracture strain, the *D*HIC decreases with the *Eloss* increase, which indicates that the larger *D*HIC, the more frequent deflection during crack propagation, thereby absorbing the energy, so the final *Eloss* is smaller. Fig. 18(d) shows the relationship between the *D*R and the *D*HIC under fracture strain. This is also consistent with the results of Kobayashi et al.'s [47] work on brittle fracture of polycrystalline nickel. In addition, this is consistent with our previous report that the *Eloss* decreases with the fracture fractal dimension increase [8]. Since HICs propagate along RGBs on a micro scale, the essence of fractal is that the fractal dimension has scale invariance, specifically, they have self-similar character at different scales and have statistical significance. In this study, the RGBs fractal character on a micro scale determine the HICs distribution on a macro scale. The fractal dimension of RGBs and HICs is the bridge connecting the HICs propagation from the macro to micro levels in TWIP steels. We know that the *FΣ3* and *FRGB* treatment are in a trade-off relationship in TWIP steels after thermomechanical. All in all, whether at the macro or micro level, increasing the *FΣ3* would fundamentally improve the hydrogen embrittlement performance. Additionally, the HIC propagation direction is approximately parallel to a trace of the {111} slip plane (Fig. 12). As all know, the planes of dislocation planar slip or deformation twining is {111} in TWIP steel, and the presence of hydrogen will further promote the dislocations or partial dislocations

planarity slip localization. These dislocations will accumulate at the grain boundaries, resulting in higher stress concentration at the grain boundaries, further leading to the grain boundaries separation with clearly visible traces on the facet of intergranular fracture surface [84, 88]. This phenomenon is similar to that previously reported in austenitic steels [89]. And the hydrogen-induced cracks will propagate once initiated. When the crack tip approaches the grain boundary plane packed by the planar slip dislocations, the crack tip stress field will further promote the slip deformation on the {111} slip plane, which makes the crack propagation direction is parallel or approximately parallel to the slip traces. This phenomenon has been similarly reported in high-entropy alloys and discussed in detail [90].

5. Conclusion

The influence of heterogeneous deformation and grain boundary character on HICs initiation and propagation in TWIP steels after thermomechanical treatment was systematically and statistically investigated by SEM, EBSD and digital image processing analyses. The primary findings of this study are summarized as follows: 1. The four specimens of TWIP steels had the almost same UTS and different grain boundary types were obtained by thermomechanical treatment. The higher the $F\Sigma 3$ grain boundaries were, the lower the *Eloss*. The typical intergranular fracture was primarily exhibited in the brittle zone on fracture surfaces; 2. The heterogeneous deformation during SSRT, i.e. the ability of slip and deformation twining to transfer across grain boundaries within both adjacent grains, is a necessary and sufficient

condition for HICs initiation. When the slip or deformation twining transfer parameter is m' less than 0.93 and the minimum residual Burgers vector of dislocations remaining on the grain boundary br is greater than 0.19, hydrogen-induced intergranular cracks will initiate at the grain boundaries. Furthermore, the slip or deformation twining are easier (or even complete) to transfer across the $\Sigma 3$ grain boundary (*Misorientation* approximately 60◦) within both adjacent grains and HICs do not initiate easily at the $\Sigma 3$ grain boundaries. RGBs create a large hindrance to slip or deformation twining transfer, which are prone to initiating HICs; 3. HICs primarily propagate along RGBs, but they can also propagate along other low-ΣCSL grain boundaries. The $\Sigma 3$ grain boundaries hinder HIC propagation or deflect HIC. The RGB fractal dimensions on a micro level determines the HIC distribution at a macro level, i.e. DHIC = 1.051DRGB + 0.465. Signifying that the more complicated the RGBs distribution is, the more irregular the HIC distribution on the specimen surface; 4. Additionally, the HIC propagation direction is approximately parallel to the trace of the {111} slip plane during the HIC propagation, which causes the slip trace to appear on the intergranular fracture facet. The heterogeneous deformation and grain boundary type of TWIP steels play decisive roles in the hydrogen-induced nucleation. Weakening the tendency of heterogeneous deformation, reducing the F_{RGB} and controlling RGB spatial distribution as well as increasing the $F_{\Sigma 3\mathrm{n}}$ (decreasing its irregularity) can effectively improve resistance to hydrogen embrittlement.

References

[1] G.-H. Zhao, X. Xu, D. Dye, P.E.J. Rivera-Díaz-del-Castillo, Microstructural evolution and strain-hardening in TWIP Ti alloys, Acta Mater. 183 (2020) 155–164, https://doi.org/10.1016/j.actamat.2019.11.009.

[2] B.C. De Cooman, Y. Estrin, S.K. Kim, Twinning-induced plasticity (TWIP) steels, Acta Mater. 142 (2018) 283–362, https://doi.org/10.1016/j.actamat.2017.06.046.

[3] J.-K. Kim, M.-H. Kwon, B.C. De Cooman, On the deformation twinning mechanisms in twinning-induced plasticity steel, Acta Mater. 141 (2017) 444–455, https://doi. org/10.1016/j.actamat.2017.09.043.

[4] S.-I. Lee, J.-M. Lee, S.-Y. Lee, H.-J. Kim, J.-Y. Suh, J.-H. Shim, U.-B. Baek, S.- H. Nahm, J. Lee, B. Hwang, Tensile and fracture behaviors of austenitic high-manganese steels subject to different hydrogen embrittlement test methods, Mater. Sci. Eng. A 766 (2019), 138367, https://doi.org/10.1016/j.msea.2019.138367.

[5] D. Wang, X. Lu, Y. Deng, X. Guo, A. Barnoush, Effect of hydrogen on nanomechanical properties in Fe-22Mn-0.6C TWIP steel revealed by in-situ electrochemical nanoindentation, Acta Mater. 166 (2019) 618–629, https://doi. org/10.1016/j.actamat.2018.12.055.

[6] I.-J. Park, S.-m Lee, H.-h Jeon, Y.-K. Lee, The advantage of grain refinement in the hydrogen embrittlement of Fe–18Mn–0.6C twinning-induced plasticity steel, Corros. Sci. 93 (2015) 63–69, https://doi.org/10.1016/j.corsci.2015.01.012.

[7] H. Fu, W. Wang, H. Zhao, F. Jin, J. Li, Study of hydrogen-induced delayed

fracture in high-Mn TWIP/TRIP steels during in situ electrochemical hydrogen-charging: role of microstructure and strain rate in crack initiation and propagation, Corros. Sci. 162 (2020), 108191, https://doi.org/10.1016/j.corsci.2019.108191.

[8] H. Fu, W. Wang, X. Chen, G. Pia, J. Li, Fractal and multifractal analysis of fracture surfaces caused by hydrogen embrittlement in high-Mn twinning/transformation-induced plasticity steels, Appl. Surf. Sci. 470 (2019) 870–881, https://doi.org/ 10.1016/j.apsusc.2018.11.179.

[9] M. Koyama, E. Akiyama, Y.-K. Lee, D. Raabe, K. Tsuzaki, Overview of hydrogen embrittlement in high-Mn steels, Int. J. Hydrog. Energy 42 (17) (2017) 12706–12723, https://doi.org/10.1016/j.ijhydene.2017.02.214.

[10] S. Ranganathan, On the geometry of coincidence-site lattices, Acta Crystallogr. 21 (2) (1966) 197–199, https://doi.org/10.1107/S0365110×66002615.

[11] D.H. Warrington, P. Bufalini, The coincidence site lattice and grain boundaries, Scr. Metall. 5 (9) (1971) 771–776, https://doi.org/10.1016/0036-9748(71)90161-X.

[12] V. Randle, The coincidence site lattice and the ‘sigma enigma’, Mater. Charact. 47 (5) (2001) 411–416, https://doi.org/10.1016/S1044-5803(02)00193-6.

[13] A. Gupta, X. Zhou, G.B. Thompson, G.J. Tucker, Role of grain boundary character and its evolution on interfacial solute segregation behavior in nanocrystalline Ni-P, Acta Mater. 190 (2020) 113–123, https://doi.org/10.1016/j.actamat.2020.03.012.

[14] L.D. Xia, Y.Z. Ji, W.B. Liu, H. Chen, Z.G. Yang, C. Zhang, L.Q. Chen, Radiation induced grain boundary segregation in ferritic/martensitic steels, Nucl. Eng.

Technol. 52 (1) (2020) 148–154, https://doi.org/10.1016/j.net.2019.07.009.

[15] C.-T. Fu, W. Yinling, X.-W. Chu, L. Jiang, W.-Z. Zhang, Q. Bai, S. Xia, B. Leng, Z.- J. Li, X.-X. Ye, F. Liu, Grain boundary engineering for control of tellurium diffusion in GH3535 alloy, J. Nucl. Mater. 497 (2017) 76–83, https://doi.org/10.1016/j.jnucmat.2017.10.052.

[16] T. Watanabe, An approach to grain-boundary design for strong and ductile polycrystals, Res Mech. 11 (1) (1984) 47–84.

[17] S. Kobayashi, R. Kobayashi, T. Watanabe, Control of grain boundary connectivity based on fractal analysis for improvement of intergranular corrosion resistance in SUS316L austenitic stainless steel, Acta Mater. 102 (2016) 397–405, https://doi. org/10.1016/j.actamat.2015.08.075.

[18] H. Fu, W. Wang, X. Chen, G. Pia, J. Li, Grain boundary design based on fractal theory to improve intergranular corrosion resistance of TWIP steels, Mater. Des. 185 (2020), 108253, https://doi.org/10.1016/j.matdes.2019.108253.

[19] T. Liu, S. Xia, T. Shoji, Q. Bai, B. Zhou, Y. Lu, The topology of three-dimensional grain boundary network and its influence on stress corrosion crack propagation characteristics in austenitic stainless steel in a simulated BWR environment, Corros. Sci. 129 (2017) 161–168, https://doi.org/10.1016/j.corsci.2017.10.003.

[20] W. Kuang, G.S. Was, C. Miller, M. Kaufman, T. Alam, B. Gwalani, R. Banerjee, The effect of cold rolling on grain boundary structure and stress corrosion cracking susceptibility of twins in alloy 690 in simulated PWR primary water

environment, Corros. Sci. 130 (2018) 126–137, https://doi.org/10.1016/j.corsci.2017.11.002.

[21] V. Thaveeprungsriporn, G.S. Was, The role of coincidence-site-lattice boundaries in creep of Ni-16Cr-9Fe at 360 ◦C, Metall. Mater. Trans. A 28 (10) (1997) 2101–2112, https://doi.org/10.1007/s11661-997-0167-6.

[22] S. Bechtle, M. Kumar, B.P. Somerday, M.E. Launey, R.O. Ritchie, Grain-boundary engineering markedly reduces susceptibility to intergranular hydrogen embrittlement in metallic materials, Acta Mater. 57 (14) (2009) 4148–4157, https://doi.org/10.1016/j.actamat.2009.05.012.

[23] Y.J. Kwon, H.J. Seo, J.N. Kim, C.S. Lee, Effect of grain boundary engineering on hydrogen embrittlement in Fe-Mn-C TWIP steel at various strain rates, Corros. Sci. 142 (2018) 213–221, https://doi.org/10.1016/j.corsci.2018.07.028.

[24] Y.J. Kwon, S.-P. Jung, B.-J. Lee, C.S. Lee, Grain boundary engineering approach to improve hydrogen embrittlement resistance in Fe Mn C TWIP steel, Int. J. Hydrog. Energy 43 (21) (2018) 10129–10140, https://doi.org/10.1016/j.ijhydene.2018.04.048.

[25] Z. Zhang, G. Obasi, R. Morana, M. Preuss, Hydrogen assisted crack initiation and propagation in a nickel-based superalloy, Acta Mater. 113 (2016) 272–283, https://doi.org/10.1016/j.actamat.2016.05.003.

[26] E.D. Merson, P.N. Myagkikh, V.A. Poluyanov, D.L. Merson, A. Vinogradov, Quasi-cleavage hydrogen-assisted cracking path investigation by fractographic and side surface observations, Eng. Fract. Mech. 214 (2019) 177–193, https://doi.org/

10.1016/j.engfracmech.2019.04.042.

[27] Z. Wang, J. Xu, J. Li, Effect of heat treatment processes on hydrogen embrittlement in hot-rolled medium Mn steels, Int. J. Hydrog. Energy 45 (2020) 20004–20020, https://doi.org/10.1016/j.ijhydene.2020.04.241.

[28] Z. Zhang, S. Xia, Q. Bai, T. Liu, H. Li, B. Zhou, L. Wang, W. Ma, Effects of 3-D grain boundary geometrical angles and the net normal stress on intergranular stress corrosion cracking initiation in a 316 stainless steel, Mater. Sci. Eng. A 765 (2019), 138277, https://doi.org/10.1016/j.msea.2019.138277.

[29] M. Jim´enez, W. Ludwig, D. Gonzalez, J.M. Molina-Aldareguia, The role of slip transfer at grain boundaries in the propagation of microstructurally short fatigue cracks in Ni-based superalloys, Scr. Mater. 162 (2019) 261–265, https://doi.org/10.1016/j.scriptamat.2018.11.008.

[30] F. Briffod, A. Bleuset, T. Shiraiwa, M. Enoki, Effect of crystallographic orientation and geometrical compatibility on fatigue crack initiation and propagation in rolled Ti-6Al-4V alloy, Acta Mater. 177 (2019) 56–67, https://doi.org/10.1016/j.actamat.2019.07.025.

[31] G. Wang, Y. Yan, J. Li, J. Huang, Y. Su, L. Qiao, Hydrogen embrittlement assessment of ultra-high strength steel 30CrMnSiNi2, Corros. Sci. 77 (2013) 273–280, https://doi.org/10.1016/j.corsci.2013.08.013.

[32] S.W. Song, J.-N. Kim, H.J. Seo, T. Lee, C.S. Lee, Effects of carbon content on the tensile and fatigue properties in hydrogen-charged Fe-17Mn-xC steels: the opposing trends, Mater. Sci. Eng. A 724 (2018) 469–476, https://doi.org/10.1016/

j.msea.2018.03.117.

[33] M. Koyama, E. Akiyama, K. Tsuzaki, D. Raabe, Hydrogen-assisted failure in a twinning-induced plasticity steel studied under in situ hydrogen charging by electron channeling contrast imaging, Acta Mater. 61 (12) (2013) 4607–4618, https://doi.org/10.1016/j.actamat.2013.04.030.

[34] T.R. Bieler, P. Eisenlohr, C. Zhang, H.J. Phukan, M.A. Crimp, Grain boundaries and interfaces in slip transfer, Curr. Opin. Solid State Mater. 18 (4) (2014) 212–226, https://doi.org/10.1016/j.cossms.2014.05.003.

[35] I.B. Tu˘gluca, M. Koyama, Y. Shimomura, B. Bal, D. Canadinc, E. Akiyama, K. Tsuzaki, Lowering strain rate simultaneously enhances carbon- and hydrogen-induced mechanical degradation in an Fe-33Mn-1.1C steel, Metall. Mater. Trans. A 50 (3) (2019) 1137–1141, https://doi.org/10.1007/s11661-018-5080-7.

[36] T.R. Bieler, R. Alizadeh, M. Pe˜na-Ortega, J. Llorca, An analysis of (the lack of) slip transfer between near-cube oriented grains in pure Al, Int. J. Plast. 118 (2019) 269–290, https://doi.org/10.1016/j.ijplas.2019.02.014.

[37] S. Haouala, R. Alizadeh, T.R. Bieler, J. Segurado, J. Llorca, Effect of slip transmission at grain boundaries in Al bicrystals, Int. J. Plast. 126 (2020), 102600, https://doi.org/10.1016/j.ijplas.2019.09.006.

[38] T.R. Bieler, P. Eisenlohr, F. Roters, D. Kumar, D.E. Mason, M.A. Crimp, D. Raabe, The role of heterogeneous deformation on damage nucleation at grain boundaries in single phase metals, Int. J. Plast. 25 (9) (2009) 1655–1683, https://doi.org/ 10.1016/j.ijplas.2008.09.002.

[39] J. Kacher, B.P. Eftink, B. Cui, I.M. Robertson, Dislocation interactions with grain boundaries, Curr. Opin. Solid State Mater. 18 (4) (2014) 227–243, https://doi.org/10.1016/j.cossms.2014.05.004.

[40] B. Kan, W. Wu, Z. Yang, J. Li, Stress-induced hydrogen redistribution and corresponding fracture behavior of Q960E steel at different hydrogen content, Mater. Sci. Eng. A 775 (2020), 138963, https://doi.org/10.1016/j. msea.2020.138963.

[41] Z. Wang, J. Xu, J. Li, Influence of microstructure on hydrogen embrittlement in hot-rolled medium Mn steels, Mater. Sci. Eng. A 780 (2020), 139147, https://doi.org/10.1016/j.msea.2020.139147.

[42] Y.P. Zhang, D.M. Shi, W.Y. Chu, L.J. Qiao, Y.L. Shi, S.L. Zheng, S.B. Wang, Hydrogen-assisted cracking of T-250 maraging steel, Mater. Sci. Eng. A 471 (1) (2007) 34–37, https://doi.org/10.1016/j.msea.2007.02.111.

[43] G. Pia, F. Delogu, Coarsening of nanoporous Au: relationship between structure and mechanical properties, Acta Mater. 99 (2015) 29–38, https://doi.org/10.1016/j.actamat.2015.07.074.

[44] G. Pia, F. Delogu, Nanoporous Au: statistical analysis of morphological features and evaluation of their influence on the elastic deformation behavior by phenomenological modeling, Acta Mater. 85 (2015) 250–260, https://doi.org/10.1016/j.actamat.2014.11.040.

[45] X. Chen, G. Yao, E. Herrero-Bervera, J. Cai, K. Zhou, C. Luo, P. Jiang, J. Lu, A new model of pore structure typing based on fractal geometry, Mar. Pet. Geol. 98 (2018) 291–305, https://doi.org/10.1016/j.marpetgeo.2018.08.023.

[46] X. Chen, G. Yao, J. Cai, Y. Huang, X. Yuan, Fractal and multifractal analysis of different hydraulic flow units based on micro-CT images, J. Nat. Gas Sci. Eng. 48 (2017) 145–156, https://doi.org/10.1016/j.jngse.2016.11.048.

[47] S. Kobayashi, T. Maruyama, S. Tsurekawa, T. Watanabe, Grain boundary engineering based on fractal analysis for control of segregation-induced intergranular brittle fracture in polycrystalline nickel, Acta Mater. 60 (17) (2012) 6200–6212, https://doi.org/10.1016/j.actamat.2012.07.065.

[48] S. Kobayashi, S. Tsurekawa, T. Watanabe, A new approach to grain boundary engineering for nanocrystalline materials, Beilstein J. Nanotechnol. 7 (2016) 1829–1849, https://doi.org/10.3762/bjnano.7.176.

[49] K.S. de Assis, C.G.C. Schuabb, M.A. Lage, M.P.P. Gonçalves, D.P. Dias, O.R. Mattos, Slow strain rate tests coupled with hydrogen permeation: new possibilities to assess the role of hydrogen in stress corrosion cracking tests part I: methodology and commissioning results, Corros. Sci. 152 (2019) 45–53, https://doi.org/10.1016/j.corsci.2019.02.028.

[50] F. Bachmann, R. Hielscher, H. Schaeben, Texture analysis with MTEX – free and open source software toolbox, Solid State Phenom. 160 (2010) 63–68, https://doi.org/10.4028/www.scientific.net/SSP.160.63.

[51] T. Watanabe, H. Fujii, H. Oikawa, K.I. Arai, Grain boundaries in rapidly solidified and annealed Fe-6.5 mass% Si polycrystalline ribbons with high ductility, Acta Metall. 37 (3) (1989) 941–952, https://doi.org/10.1016/0001-6160(89)90021-7.

[52] D.G. Brandon, The structure of high-angle grain boundaries, Acta Metall. 14

(11) (1966) 1479–1484, https://doi.org/10.1016/0001-6160(66)90168-4.

[53] Y. Su, C. Zambaldi, D. Mercier, P. Eisenlohr, T.R. Bieler, M.A. Crimp, Quantifying deformation processes near grain boundaries in α titanium using nanoindentation and crystal plasticity modeling, Int. J. Plast. 86 (2016) 170–186, https://doi.org/ 10.1016/j.ijplas.2016.08.007.

[54] B.E. Dunlap, Investigation of Single Crystal and Bi-Crystal Deformation in Body- Centered Cubic Tantalum Using Indentation, Michigan State University, 2018.

[55] X. Chen, G. Yao, An improved model for permeability estimation in low permeable porous media based on fractal geometry and modified Hagen-Poiseuille flow, Fuel 210 (2017) 748–757, https://doi.org/10.1016/j.fuel.2017.08.101.

[56] ´E. Martin, W. Muhammad, A.J. Detor, I. Spinelli, A. Wessman, D. Wei, Strain-annealed" grain boundary engineering process investigated in Hastelloy-X, Materialia 9 (2020), 100544, https://doi.org/10.1016/j.mtla.2019.100544.

[57] J.T. Tan, B.K. Chen, Coalescence and growth of two coplanar short cracks in AA7050-T7451 aluminium alloys, Eng. Fract. Mech. 102 (2013) 324–333, https:// doi.org/10.1016/j.engfracmech.2013.03.002.

[58] F. Huq, J. Liu, A.L. Tonge, L. Graham-Brady, A micromechanics based model to predict micro-crack coalescence in brittle materials under dynamic compression, Eng. Fract. Mech. 217 (2019), 106515, https://doi.org/10.1016/j. engfracmech.2019.106515.

[59] J. Luster, M.A. Morris, Compatibility of deformation in two-phase Ti-Al alloys: dependence on microstructure and orientation relationships, Metall. Mater. Trans. A 26 (7) (1995) 1745–1756, https://doi.org/10.1007/BF02670762.

[60] H. Idrissi, K. Renard, L. Ryelandt, D. Schryvers, P.J. Jacques, On the mechanism of twin formation in Fe–Mn–C TWIP steels, Acta Mater. 58 (7) (2010) 2464–2476, https://doi.org/10.1016/j.actamat.2009.12.032.

[61] J.W. Christian, S. Mahajan, Deformation twinning, Prog. Mater. Sci. 39 (1) (1995) 1–157, https://doi.org/10.1016/0079-6425(94)00007-7.

[62] E. Bayerschen, A.T. McBride, B.D. Reddy, T. B¨ohlke, Review on slip transmission criteria in experiments and crystal plasticity models, J. Mater. Sci. 51 (5) (2016) 2243–2258, https://doi.org/10.1007/s10853-015-9553-4.

[63] T.C. Lee, I.M. Robertson, H.K. Birnbaum, An in situ transmission electron microscope deformation study of the slip transfer mechanisms in metals, Metall. Trans. A 21 (9) (1990) 2437–2447, https://doi.org/10.1007/BF02646988.

[64] I. Gutierrez-Urrutia, D. Raabe, Dislocation and twin substructure evolution during strain hardening of an Fe–22wt% Mn–0.6wt% C TWIP steel observed by electron channeling contrast imaging, Acta Mater. 59 (16) (2011) 6449–6462, https://doi. org/10.1016/j.actamat.2011.07.009.

[65] A.E. Pontini, J.D. Hermida, X-ray diffraction measurement of the stacking fault energy reduction induced by hydrogen in an AISI 304 steel, Scr. Mater. 37 (11) (1997) 1831–1837, https://doi.org/10.1016/S1359-6462(97)00332-1.

[66] H. Grimmer, Coincidence-site lattices, Acta Crystallogr. A 32 (5) (1976) 783–785, https://doi.org/10.1107/S056773947601231X.

[67] H. Grimmer, W. Bollmann, D.H. Warrington, Coincidence-site lattices and complete pattern-shift in cubic crystals, Acta Crystallogr. A 30 (2) (1974) 197–207,

https://doi.org/10.1107/S056773947400043X.

[68] R. Alizadeh, M. Pe˜na-Ortega, T.R. Bieler, J. Llorca, A criterion for slip transfer at grain boundaries in Al, Scr. Mater. 178 (2020) 408–412, https://doi.org/10.1016/ j.scriptamat.2019.12.010.

[69] I.M. Robertson, H.K. Birnbaum, P. Sofronis, Chapter 91 hydrogen effects on plasticity, in: J.P. Hirth, L. Kubin (Eds.), Dislocations in Solids, Elsevier, 2009, pp. 249–293.

[70] P. Sofronis, H.K. Birnbaum, Mechanics of the hydrogendashdislocationdashimpurity interactions—I. Increasing shear modulus, J. Mech. Phys. Solids 43 (1) (1995) 49–90, https://doi.org/10.1016/0022-5096 (94)00056-B.

[71] R. Kirchheim, B. Somerday, P. Sofronis, Chemomechanical effects on the separation of interfaces occurring during fracture with emphasis on the hydrogen-iron and hydrogen-nickel system, Acta Mater. 99 (2015) 87–98, https://doi.org/ 10.1016/j.actamat.2015.07.057.

[72] R. Kirchheim, Reducing grain boundary, dislocation line and vacancy formation energies by solute segregation. I. Theoretical background, Acta Mater. 55 (15) (2007) 5129–5138, https://doi.org/10.1016/j.actamat.2007.05.047.

[73] A.H. Cottrell, Theory of dislocations, Prog. Met. Phys. 4 (1953) 205–264, https:// doi.org/10.1016/0502-8205(53)90018-5.

[74] R.A. Oriani, Whitney award lecture—1987: hydrogen—the versatile embrittler, Corrosion 43 (7) (1987) 390–397, https://doi.org/10.5006/1.3583875.

[75] R.A. Oriani, P.H. Josephic, Hydrogen-enhanced load relaxation in a deformed medium-carbon steel, Acta Metall. 27 (6) (1979) 997–1005, https://doi.org/10.1016/0001-6160(79)90187-1.

[76] J.P. Hirth, Effects of hydrogen on the properties of iron and steel, Metall. Trans. A 11 (6) (1980) 861–890, https://doi.org/10.1007/BF02654700.

[77] S.-M. Lee, I.-J. Park, J.-G. Jung, Y.-K. Lee, The effect of Si on hydrogen embrittlement of Fe-18Mn-0.6C-xSi twinning-induced plasticity steels, Acta Mater. 103 (2016) 264–272, https://doi.org/10.1016/j.actamat.2015.10.015.

[78] G.M. Pressouyre, A classification of hydrogen traps in steel, Metall. Trans. A 10 (10) (1979) 1571–1573, https://doi.org/10.1007/BF02812023.

[79] K.S. de Assis, M.A. Lage, G. Guttemberg, F.P. dos Santos, O.R. Mattos, Influence of hydrogen on plasticity around the crack tip in high strength steels, Eng. Fract. Mech. 176 (2017) 116–125, https://doi.org/10.1016/j.engfracmech.2017.02.028.

[80] W. Bollmann, Crystal Defects and Crystalline Interfaces, Springer Science & Business Media, 2012.

[81] X. Tao, G.-C. Lv, J. Kou, X. Xiong, A.A. Volinsky, C.-S. Ku, K. Chen, Y.-J. Su, Synchrotron X-ray Laue diffraction study of hydrogen-induced blisters on iron grain boundaries, Scr. Mater. 169 (2019) 82–86, https://doi.org/10.1016/j.scriptamat.2019.05.009.

[82] Z. Zheng, D.S. Balint, F.P.E. Dunne, Investigation of slip transfer across HCP grain boundaries with application to cold dwell facet fatigue, Acta Mater. 127 (2017) 43–53, https://doi.org/10.1016/j.actamat.2017.01.021.

[83] D.E. Spearot, M.D. Sangid, Insights on slip transmission at grain boundaries from atomistic simulations, Curr. Opin. Solid State Mater. 18 (4) (2014) 188–195, https://doi.org/10.1016/j.cossms.2014.04.001.

[84] G. Han, J. He, S. Fukuyama, K. Yokogawa, Effect of strain-induced martensite on hydrogen environment embrittlement of sensitized austenitic stainless steels at low temperatures, Acta Mater. 46 (13) (1998) 4559–4570, https://doi.org/10.1016/ S1359-6454(98)00136-0.

[85] B. An, H. Itouga, T. Iijima, C. San Marchi, B. Somerday, Hydrogen-Assisted Twin Boundary Fracture of Type 304 Austenitic Stainless Steel at Low Temperature Investigated by Scanning Probe Microscopy, 2013.

[86] L.W. Tsay, M.C. Young, C. Chen, Fatigue crack growth behavior of laser-processed 304 stainless steel in air and gaseous hydrogen, Corros. Sci. 45 (9) (2003) 1985–1997, https://doi.org/10.1016/S0010-938X(03)00036-2.

[87] S. Ueki, Y. Mine, K. Takashima, Crystallographic study of hydrogen-induced twin boundary separation in type 304 stainless steel under cyclic loading, Corros. Sci. 129 (2017) 205–213, https://doi.org/10.1016/j.corsci.2017.10.013.

[88] J.P. Chateau, D. Delafosse, T. Magnin, Numerical simulations of hydrogen–dislocation interactions in fcc stainless steels: part II: hydrogen effects on crack tip plasticity at a stress corrosion crack, Acta Mater. 50 (6) (2002) 1523–1538, https://doi.org/10.1016/S1359-6454(02)00009-5.

[89] T. Michler, C. San Marchi, J. Naumann, S. Weber, M. Martin, Hydrogen environment embrittlement of stable austenitic steels, Int. J. Hydrog. Energy 37 (21)

(2012) 16231–16246, https://doi.org/10.1016/j.ijhydene.2012.08.071.

[90] K. Suzuki, M. Koyama, S. Hamada, K. Tsuzaki, H. Noguchi, Planar slip-driven fatigue crack initiation and propagation in an equiatomic CrMnFeCoNi high-entropy alloy, Int. J. Fatigue 133 (2020), 105418, https://doi.org/10.1016/j.ijfatigue.2019.105418.

Acknowledgments

This project was supported by the National Natural Science Foundation of China under Grant Nos. U1760203 and 52071016.

Figures and Captions

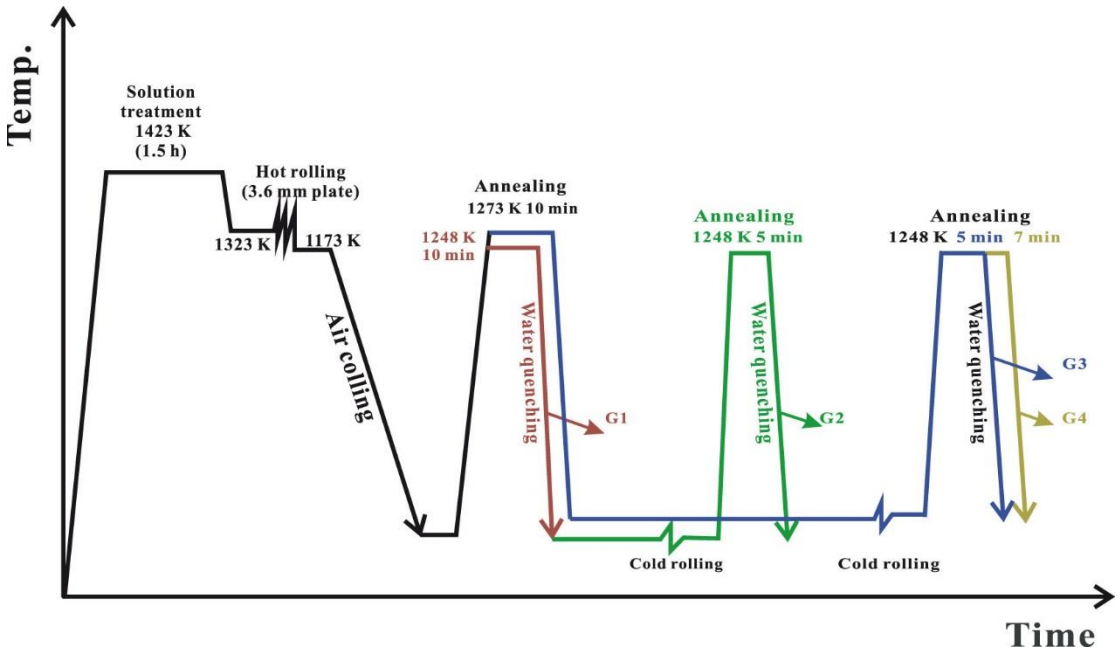

Fig. 1 Schematic diagram showing rolling and heat treatment processes.

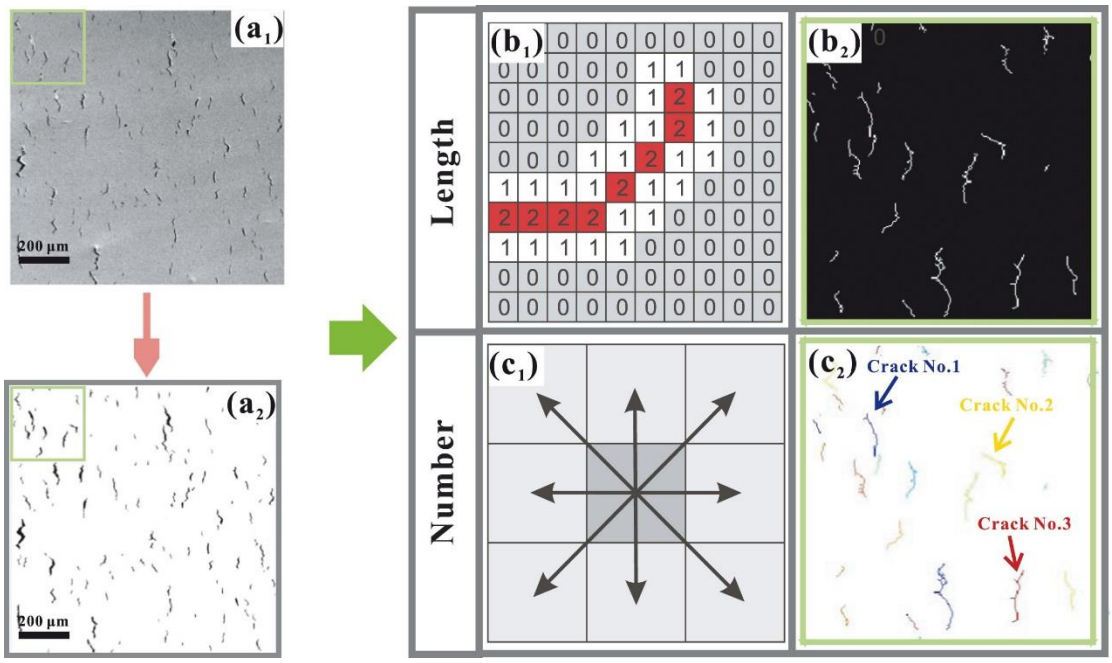

Fig. 2 Schematic diagram of HIC statistics. (a) SEM image binarization; (b) schematic of the medial axis algorithm and HIC skeleton extraction; (c) principle underlying the 8-connectivity algorithm and HICs segmentation skeleton. (For interpretation of the references to color in this figure, the reader is referred to the web version of this article.)

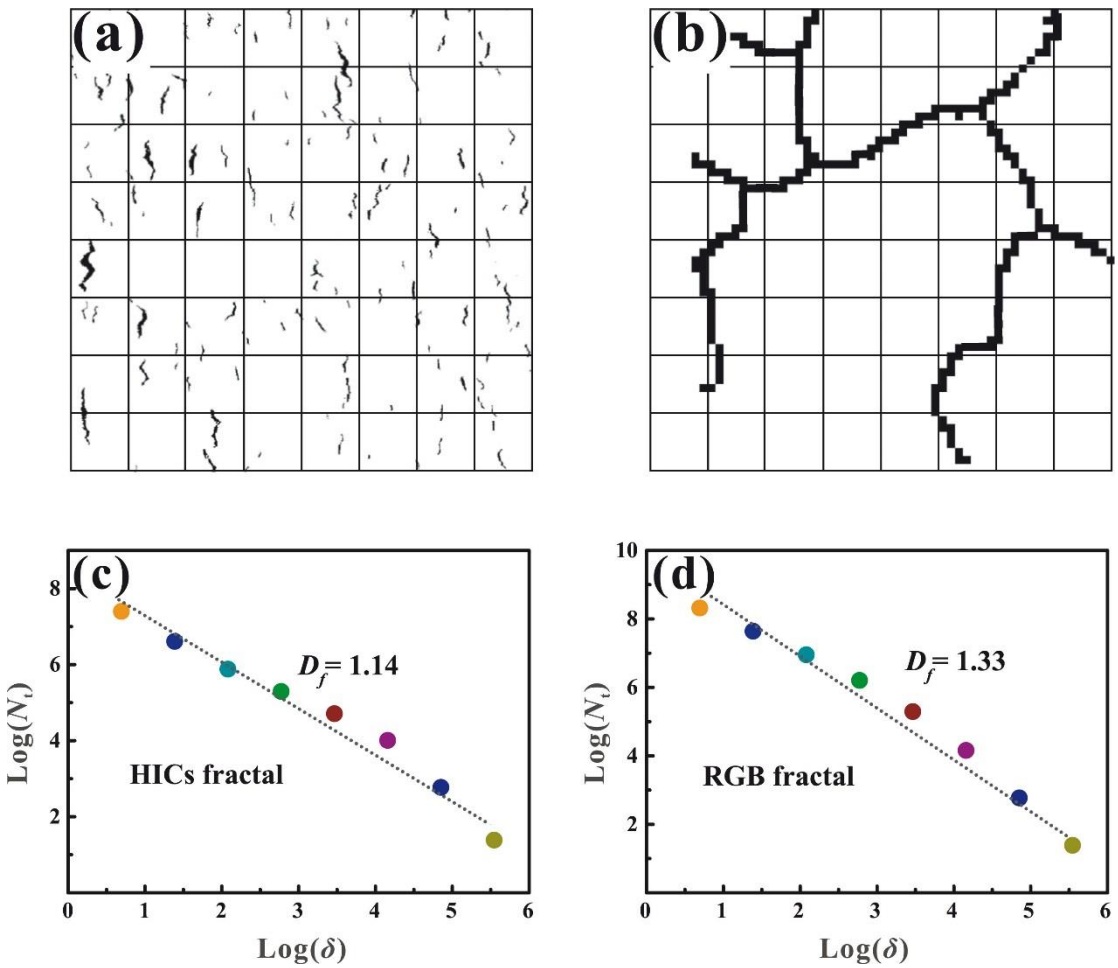

Fig. 3 Schematic diagram on the calculation method for fractal dimensions of HICs and RGB; box-counting dimension method diagram for HICs (a) and RGBs (b); and the double logarithm of the box size (δ) and the number (N_t) of HICs (c) and (d).

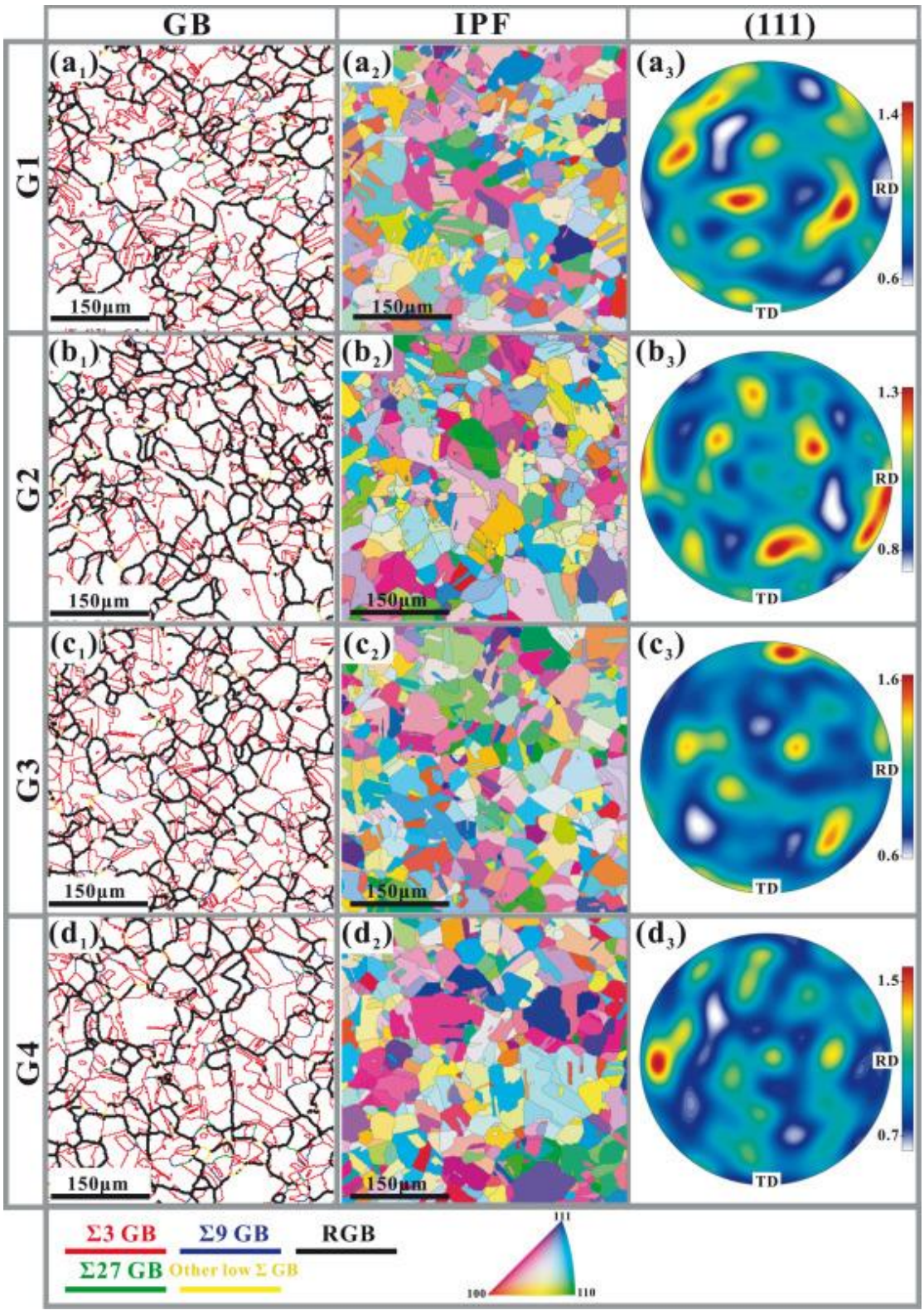

Fig. 4 Microstructure distribution character of G(1–4) specimens: (a1–d1) is the grain boundaries distribution map; (a2–d2) is the inverse pole figure (IPF); and (a3–d3) is the (111) plane pole figure diagram. (For interpretation of the references to color in this figure, the reader is referred to the web version of this article.)

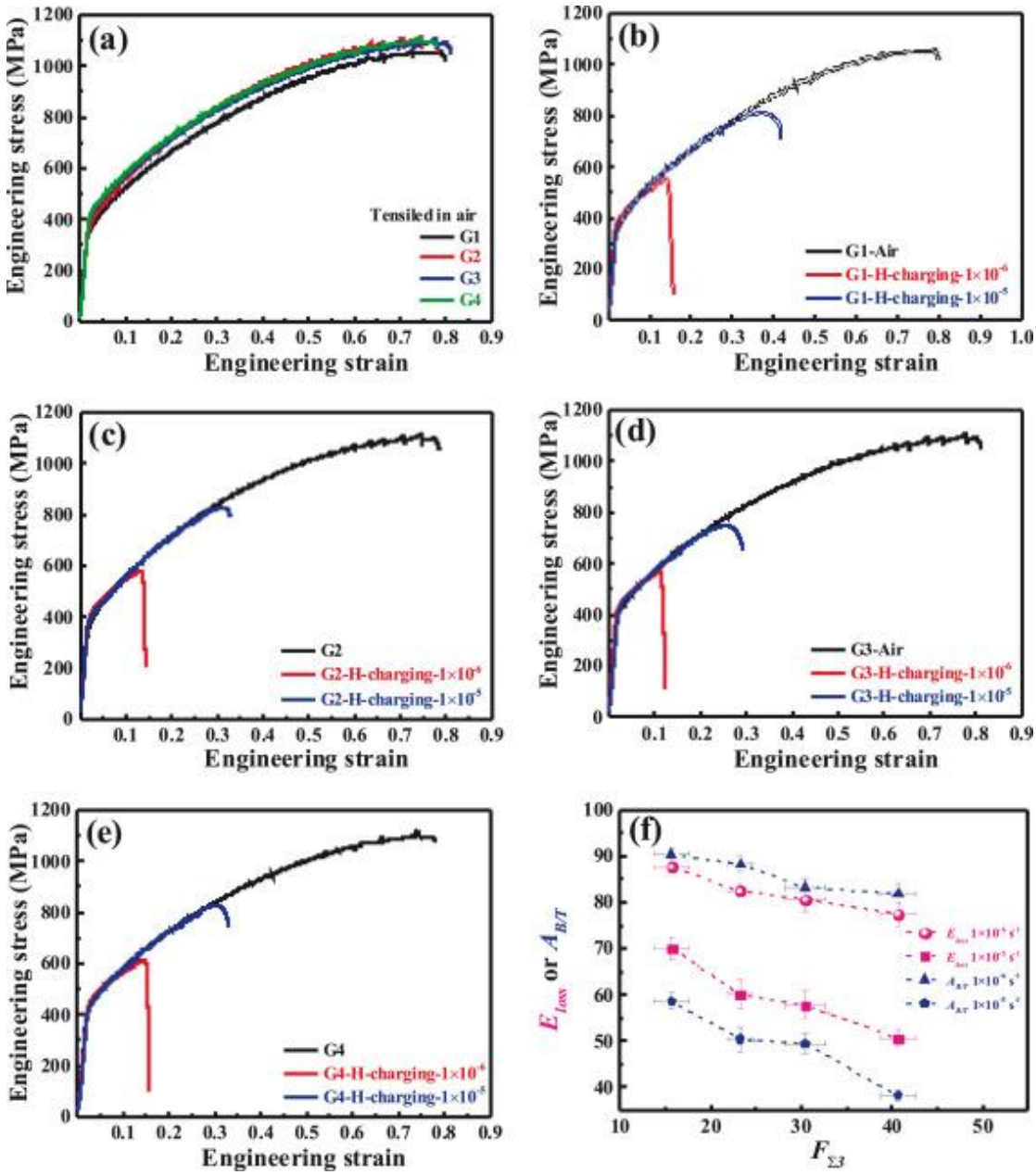

Fig. 5 Engineering stress-strain curves for the four specimens in air (a) and after the SSRT test at two different strain rates with in situ hydrogen-charging (b–d): (b) G1, (c) G2, (d) G3, and (e) G4 (in b–e, the black curve represents the engineering stress-strain curves obtained in air), (f) the relationship figure between E_{loss} or $A_{B/T}$ and $F_{\Sigma 3}$. (For interpretation of the references to color in this figure, the reader is referred to the web version of this article.)

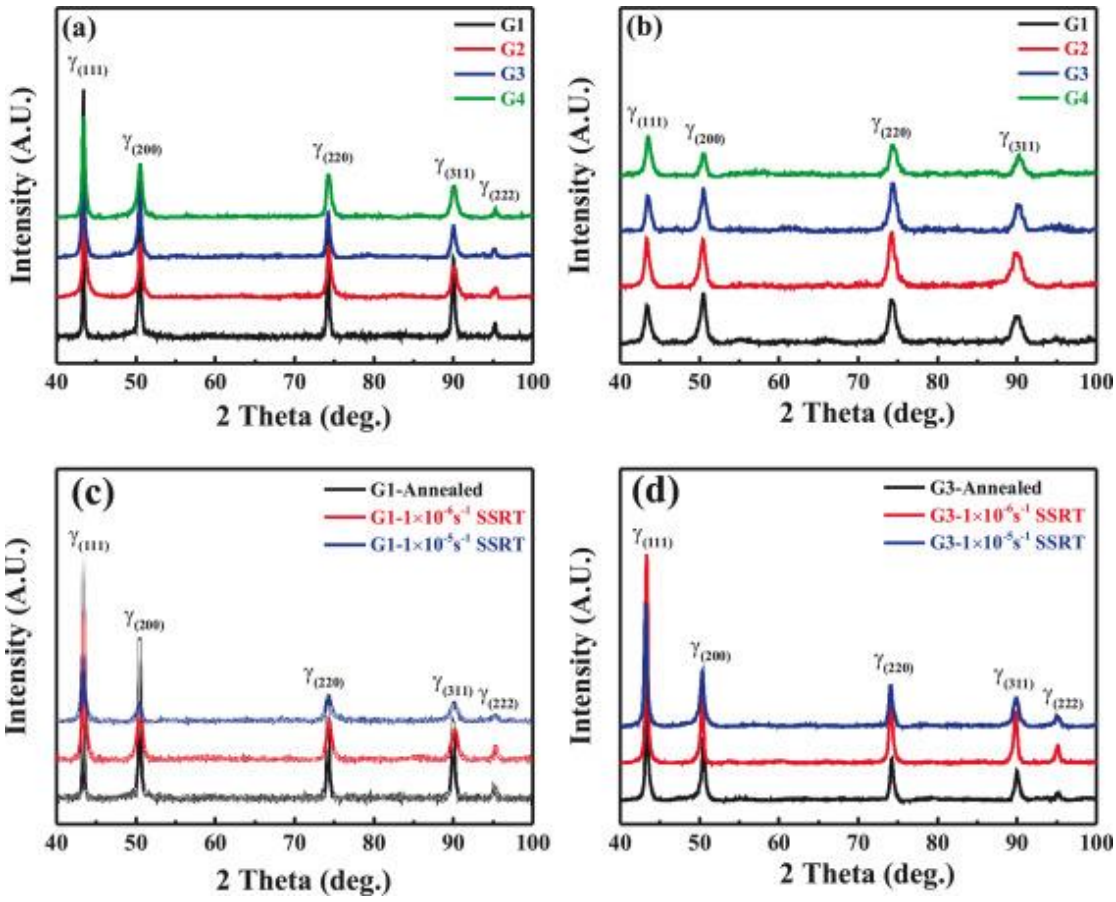

Fig. 6 (a, b) shows the XRD patterns of these specimens before and after SSRT in air, which indicates that TWIP steels can maintain their austenite phase stability. For the two specimens with the lowest and highest Eloss (G1 and G3), they did not undergo martensite transformation and could still maintain austenite stability before and after SSRT with hydrogen-charging Fig. 6(c, d).

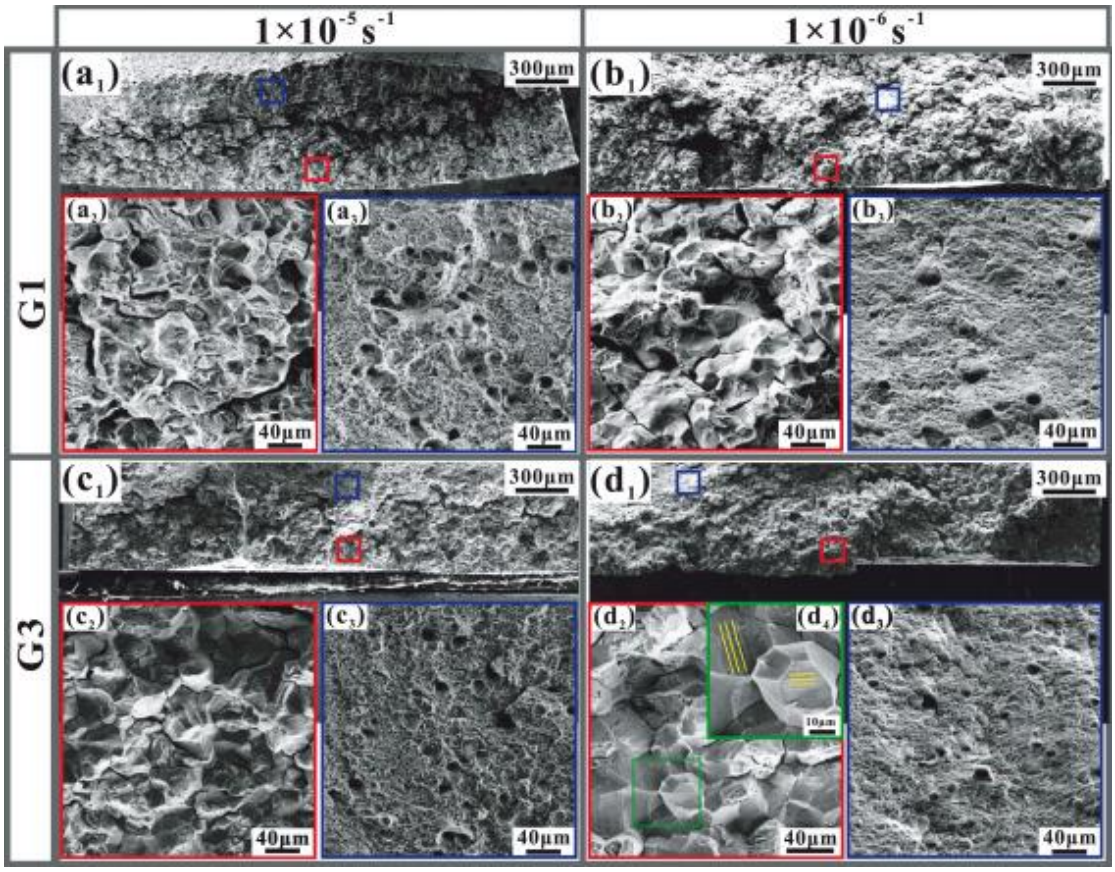

Fig. 7 Fracture surface morphology of G1 and G3 specimens after SSRT with in situ hydrogen charging at two different strain rates: (a, c) 1×10^{-6} s^{-1}; (b, d) 1×10^{-5} s^{-1}; ((a_1, b_1, c_1, and d_1) is the macroscopic fracture morphology; (a_2, b_2, c_2, and d_2) is the intergranular fracture morphology that corresponds to the local enlargement of (a_1–d_1) in the red box); (b_3, c_3, and d_3) is the ductile fracture morphology that correspond to the local enlargement of (a_1–d_1) in the blue box; and (d_4) is the local enlargement of the green box in d_3. (For interpretation of the references to color in this figure legend, the reader is referred to the web version of this article.)

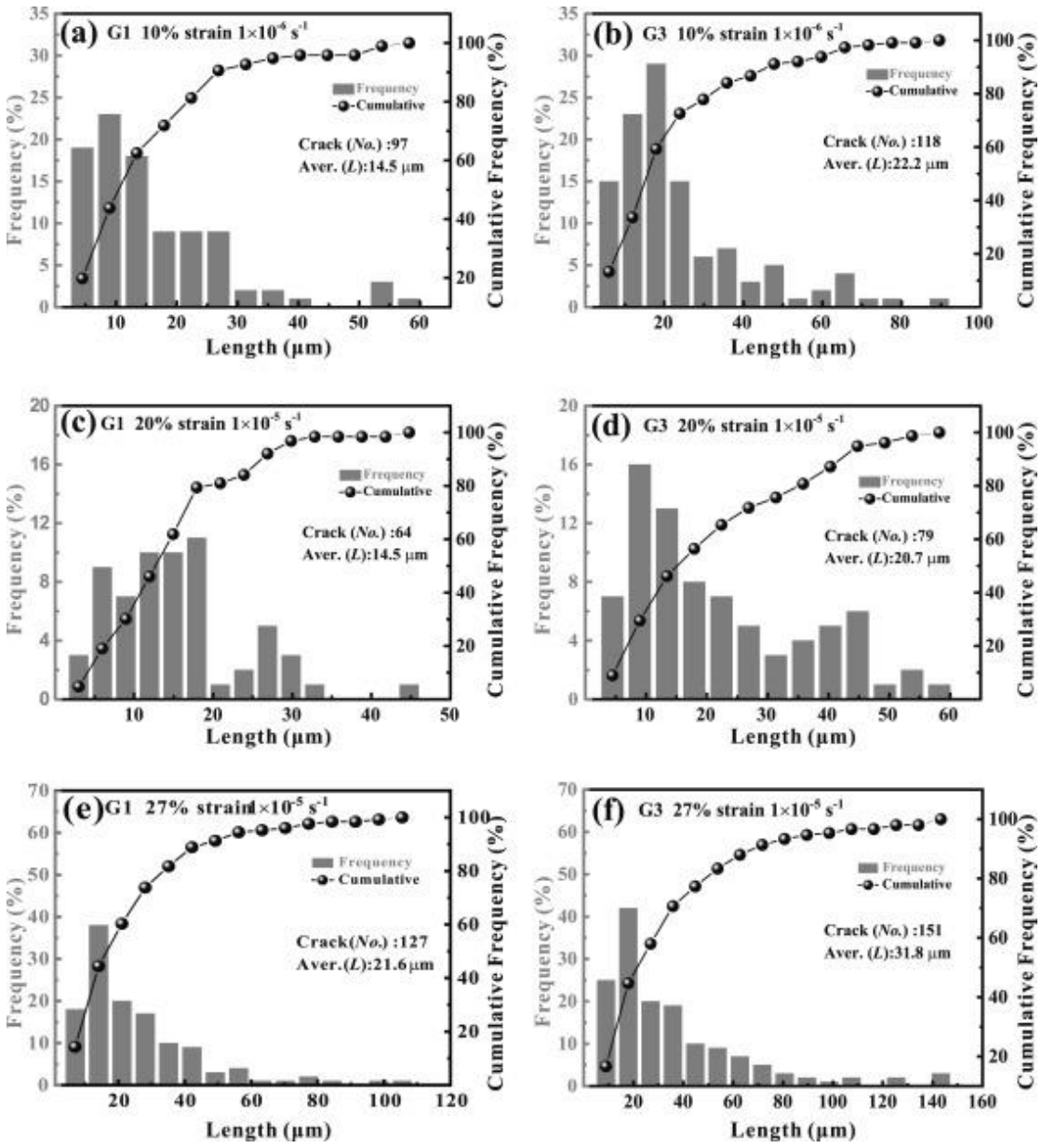

Fig. 8 Statistical histogram and cumulative frequency curve of HIC lengths for the G1 and G3 specimens when the SSRT was performed for a certain strain with in situ hydrogen-charging at two different strain rates; (a and b) 10% strain at 1×10^{-6} s^{-1}; (c, d) 20% strain at 1×10^{-5} s^{-1}; and (e, f) 27% strain at 1×10^{-5} s^{-1}.

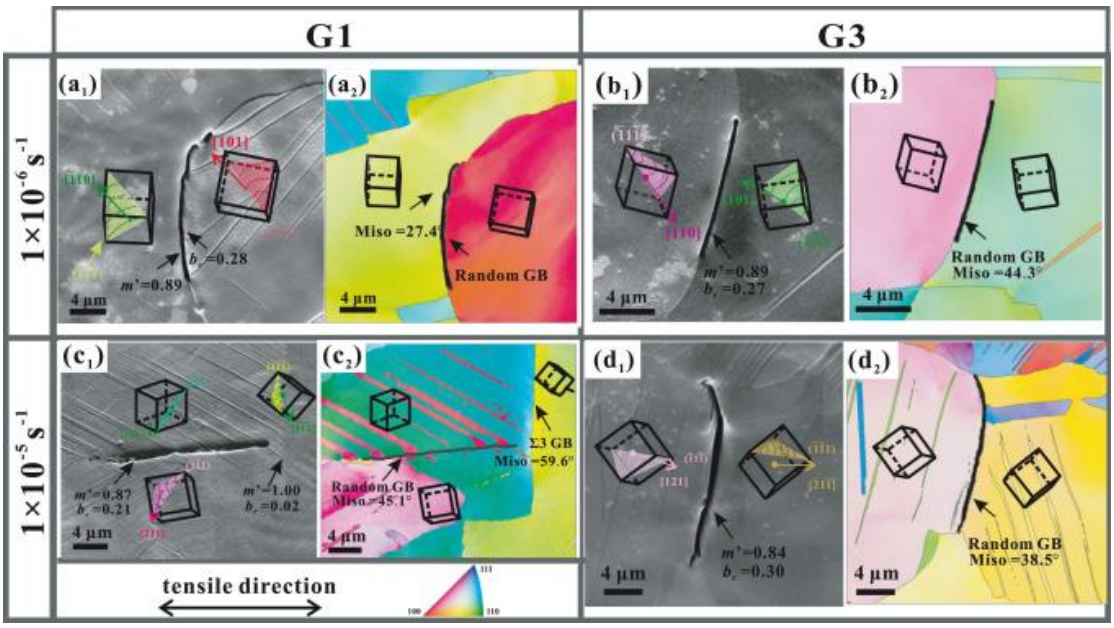

Fig. 9 SEM and EBSD maps of HICs initiation for G1 and G3 specimens with in situ hydrogen-charging at two strain rates, with (a, b) 1×10^{-6} s^{-1}; (c, d) 1×10^{-5} s^{-1}; and ((a_1–d_1) are SEM maps; and (a_2–d_2) are IPF, "Miso" represents Misorientation).

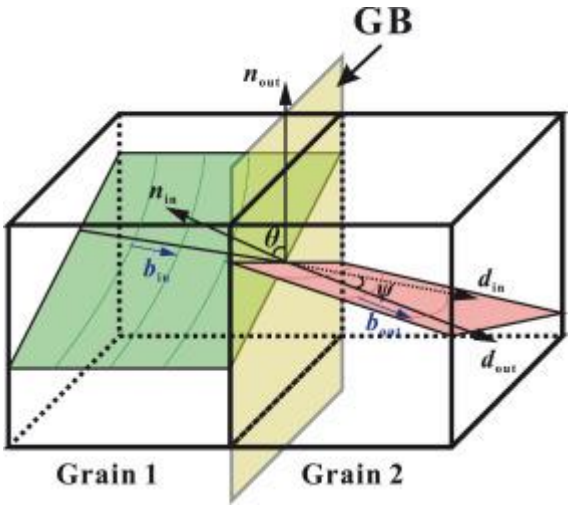

Fig. 10 Schematic of the normal unit and direction vectors of two slip systems within adjacent grains.

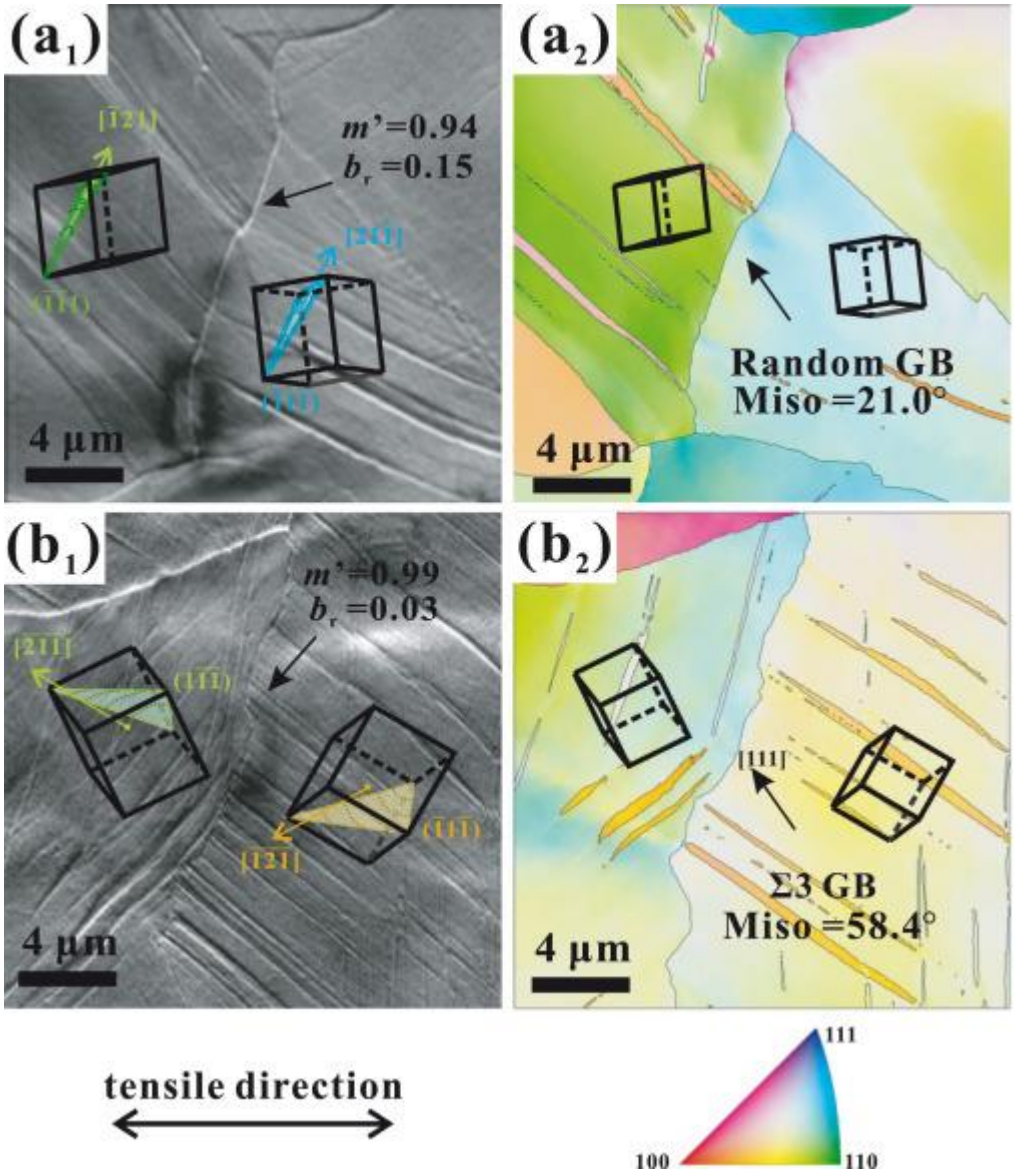

Fig. 11 SEM and EBSD maps of non-cracked grain boundaries for G1 and G3 specimens with in situ hydrogen-charging at 1×10^{-5} s^{-1} strain rates: (a) G1; (b) G3; ((a_1, b_1) are SEM maps; and (a_2, b_2) are IPF, "Miso" represents Misorientation).

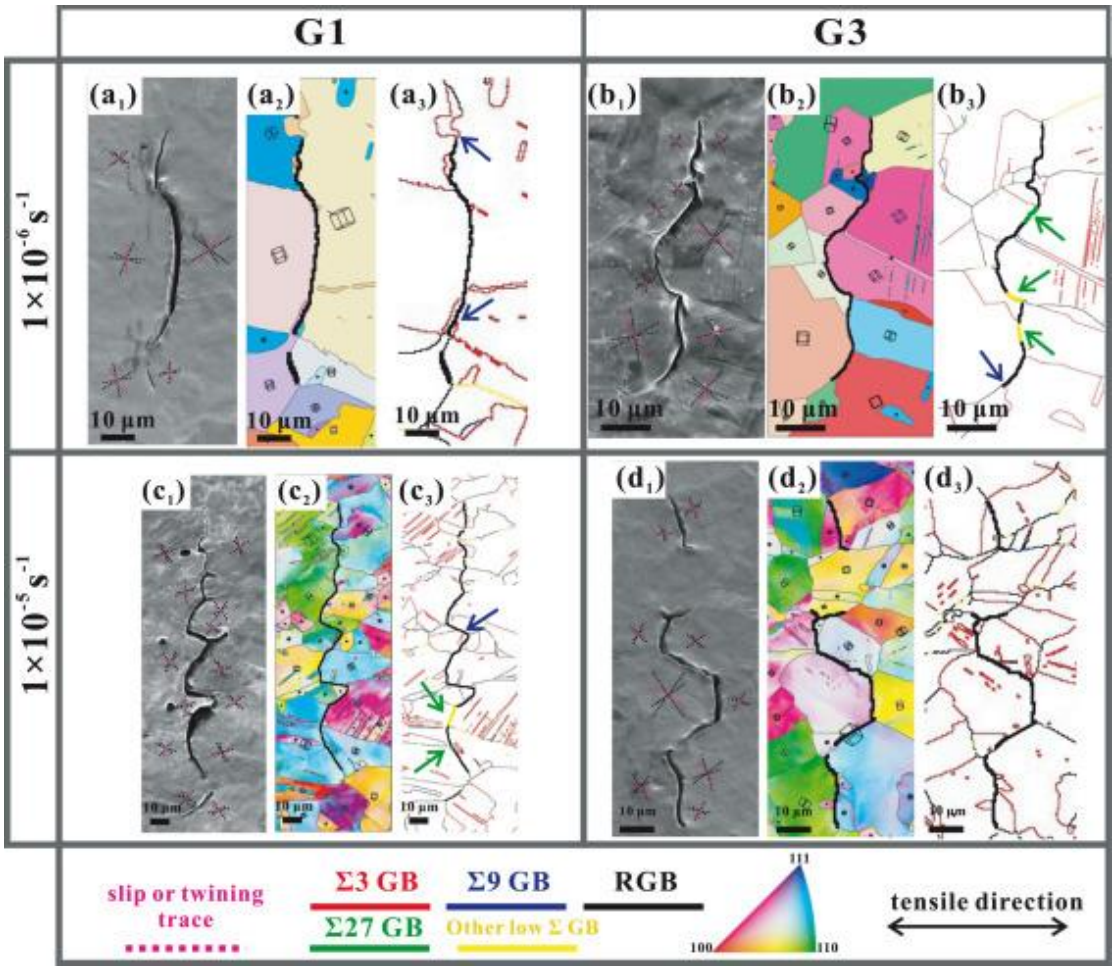

Fig. 12 SEM and EBSD maps of HIC propagation for G1 and G3 specimens with in situ hydrogen-charging at two strain rates: (a, b) G1 (c, d) G3 (for each crack was shown the SEM map (a_1–d_1), and IPF (a_3–d_4)).

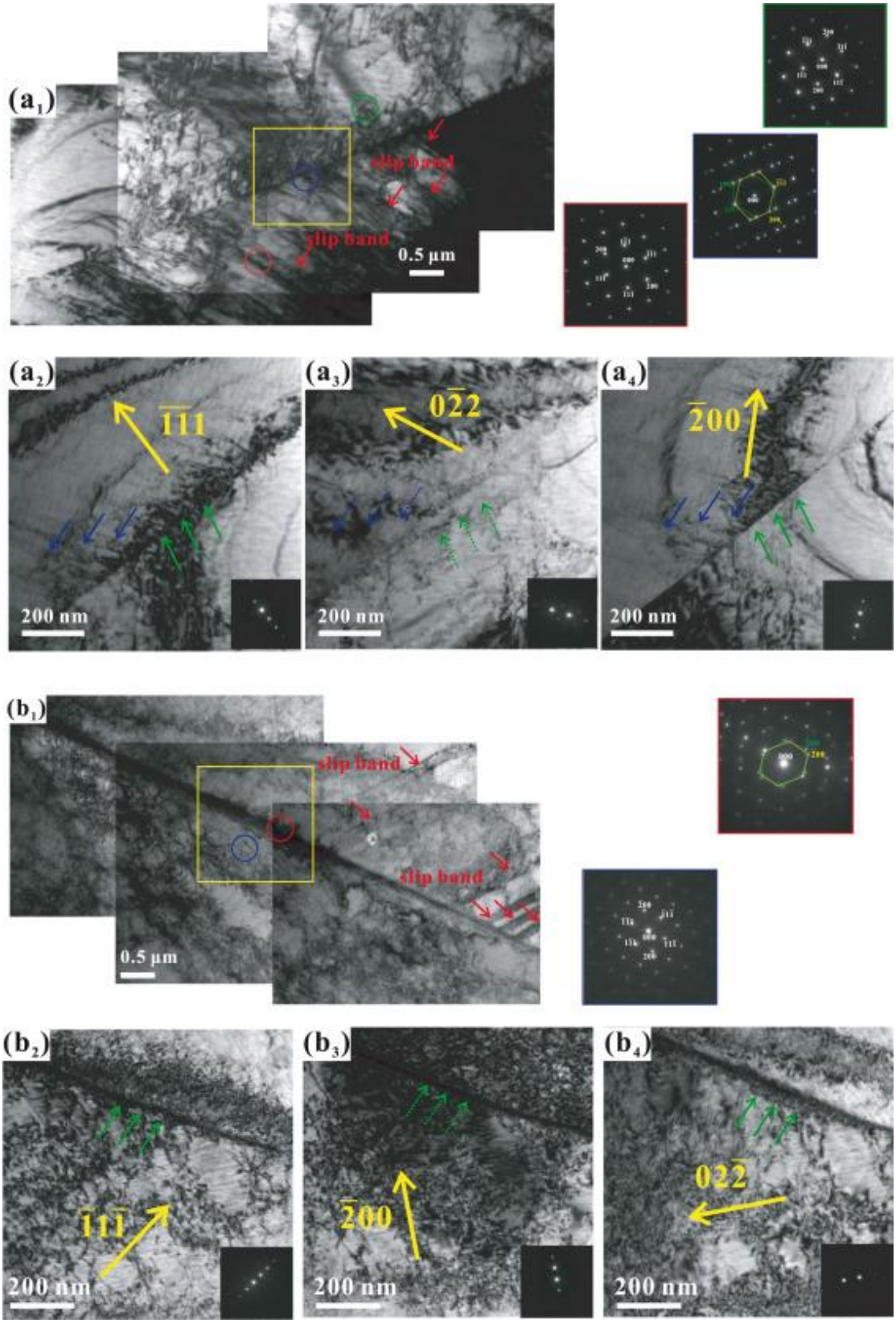

Fig. 13 TEM images of G1 and G3 specimens when the SSRT was performed at a 10% strain with in situ hydrogen-charging at a 1×10^{-6} s^{-1} strain rate for the (a) G1 specimen and (b) G3 specimen (the red, green and blue boxes correspond to the selected area diffraction patterns of the respective circle positions, and (a_2–a_4) and (b_2–b_4) are the enlarged images in the yellow boxes in (a_1) and (b_1)

respectively).

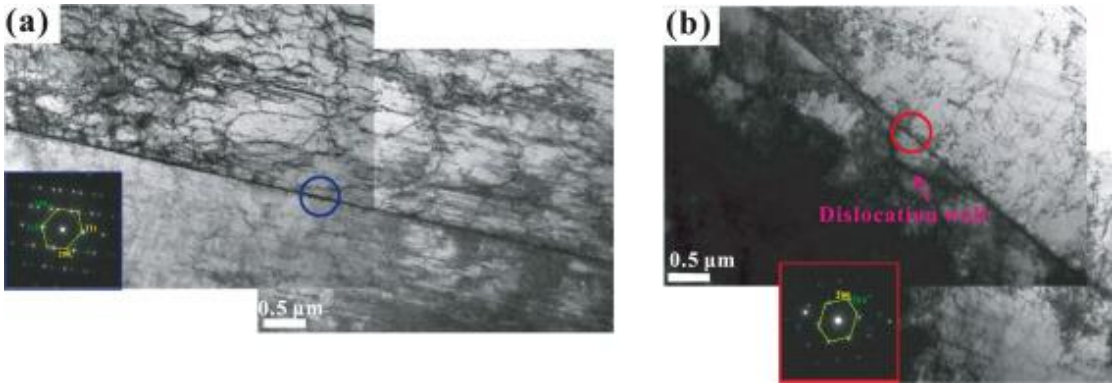

Fig. 14 TEM images of G1 and G3 specimens when the SSRT was performed at a 10% strain with hydrogen-free at a 1×10^{-6} s^{-1} strain rate for the (a) G1 specimen and (b) G3 specimen (the red and blue boxes correspond to the selected area diffraction patterns of the respective circle positions).

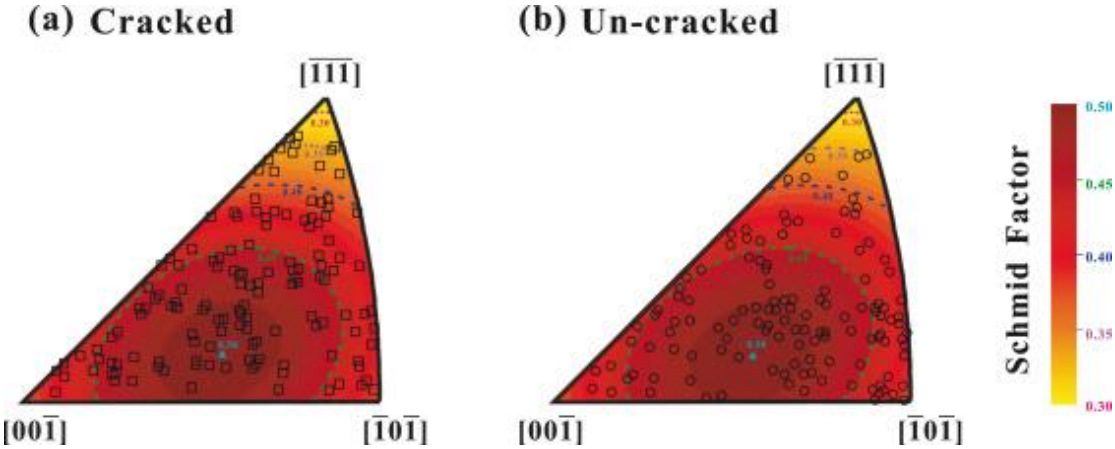

Fig. 15 Inverse pole figure along the loading direction of the crystal orientation for (a) cracked grains and (b) non-cracked grains.

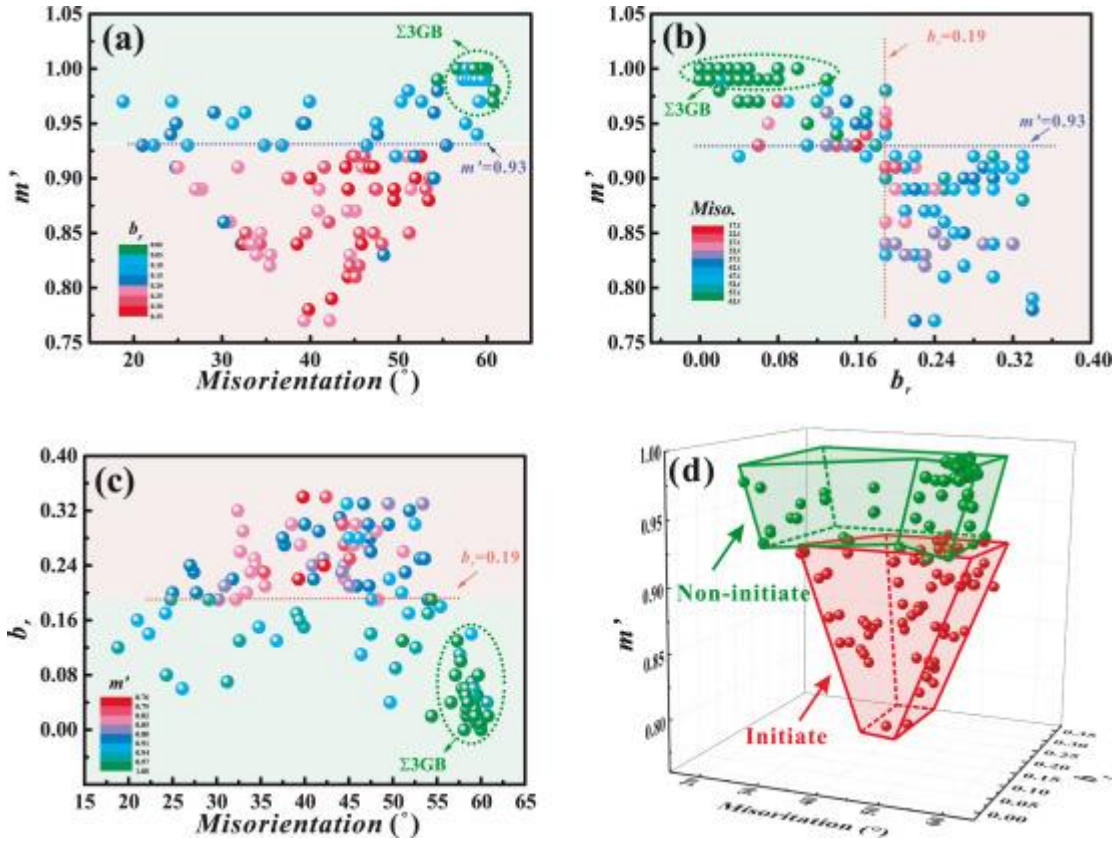

Fig. 16 Summary of statistical results on the *Misorientation*, b_r and m' of 131 grain boundaries (67 cracked and 64 non-cracked grain boundaries): (a) *Misorientation* vs. m', (b) b_r vs. m', (c) *Misorientation* vs. b_r, (d) the three-dimensional image of *Misorientation*, b_r and m' (In (a–c), the data points in the red background are cracked grain boundaries the green background are un-cracked grain boundaries; in (d), red areas are prone to cracking and the green areas are less prone to cracking). (For interpretation of the references to color in this figure legend, the reader is referred to the web version of this article.)

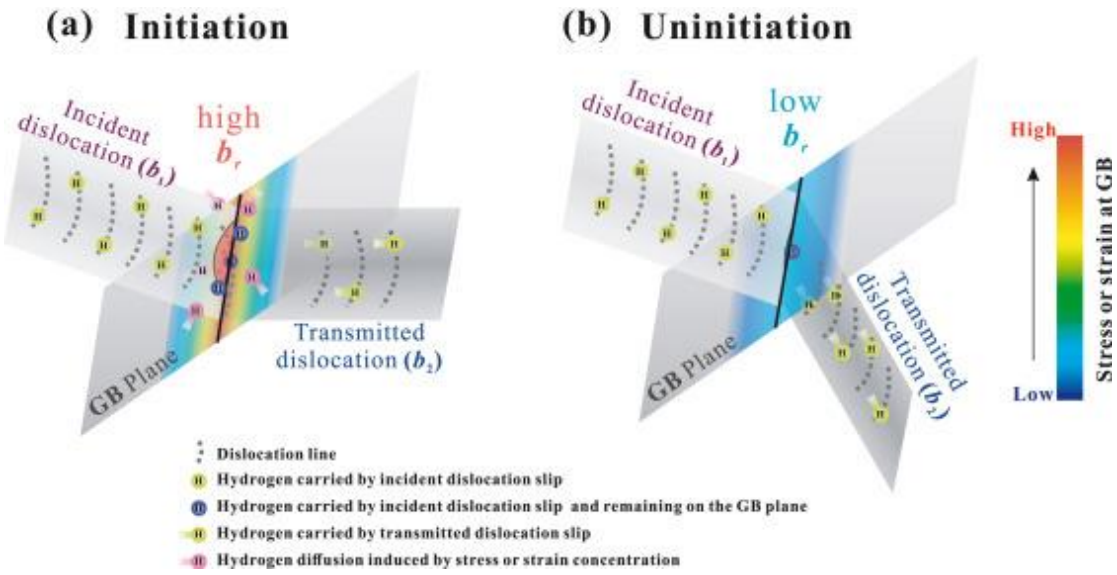

Fig. 17 Schematic diagram of hydrogen-induced cracking mechanism in TWIP steels: (a) initiation and (b) non-initiation.

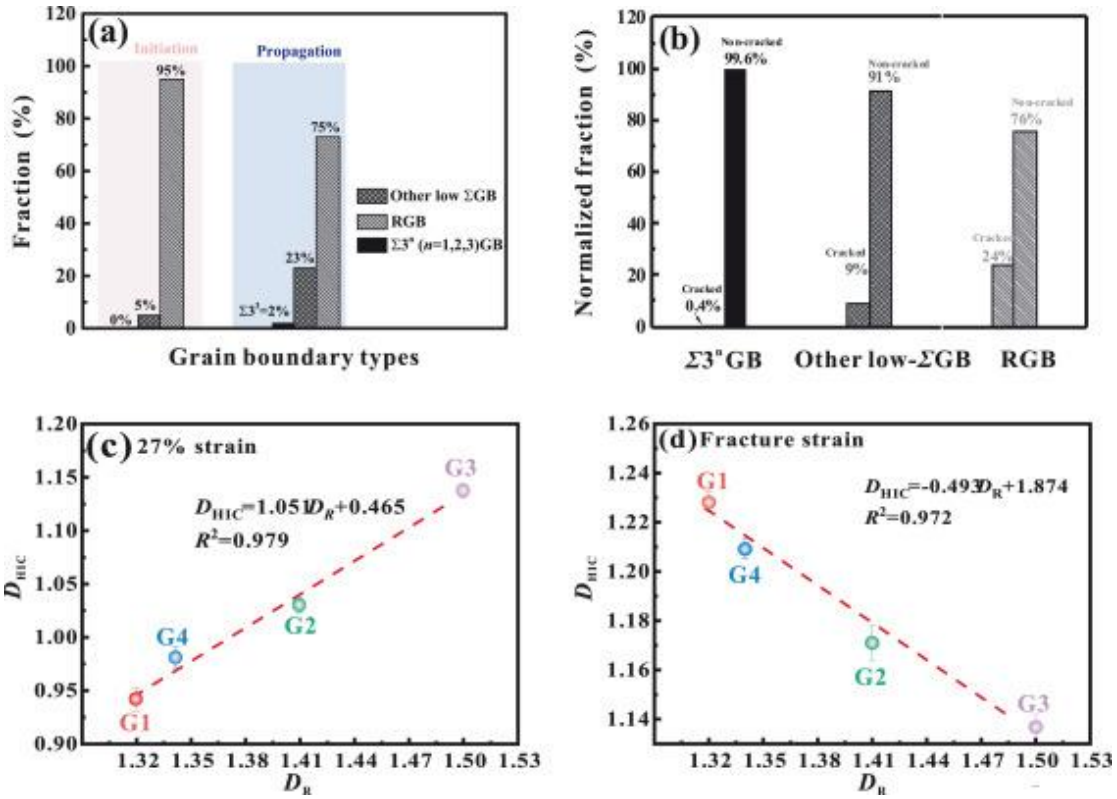

Fig. 18. (a) The fraction of different types of grain boundaries that experienced initiation and propagation; (b) normalized cracked fraction of each grain boundary type; (c, d) the relationship between the RGB fractal dimension and the HIC fractal dimension under 27% strain (c) and fracture strain (d).

Table 1 Chemical composition analysis of the steel investigated in the present study (wt.%).

Mn	C	S	P	Fe
18.2	0.56	0.006	0.008	Balance.

Table 2 Summaries on the different grain boundary types fractions, fractal of RGB and average grain size for all specimens. (Values with the standard deviation).

Specimens	$F_{\Sigma 3n}$	$F_{\Sigma 3}$	F_R	D_R	d_{ave} (μm)
G1	47.29 ± 1.53	40.69 ± 1.90	51.45 ± 1.72	1.33	23.6 ± 0.8
G2	26.65 ± 1.12	23.26 ± 1.35	72.63 ± 1.24	1.41	21.8 ± 1.3
G3	17.88 ± 2.09	15.69 ± 1.89	81.58 ± 2.12	1.50	25.2 ± 1.0
G4	33.81 ± 1.65	30.42 ± 2.23	65.06 ± 1.92	1.34	26.5 ± 1.7

Table 3 Hydrogen embrittlement susceptibility (E_{loss}) and fraction of brittle area ($A_{B/T}$) for four specimens at two strain rates. (Values with the standard deviation).

Specimens	**G1**		**G2**		**G3**		**G4**	
(%)	E_{loss}	$A_{B/T}$	E_{loss}	$A_{B/T}$	E_{loss}	$A_{B/T}$	E_{loss}	$A_{B/T}$
1×10^{-6} s^{-1}	77.5 ± 2.6	81.9 ± 1.9	82.4 ± 1.4	88.2 ± 1.6	87.6 ± 1.1	90.4 ± 1.3	80.7% ± 2.8	83.2 ± 2.1
1×10^{-5} s^{-1}	50.6 ± 1.8	32.8 ± 1.3	60.1 ± 3.1	50.4 ± 2.4	70.1 ± 2.3	58.6 ± 1.9	57.7% ± 3.0	49.4 ± 2.2

Table 4 Fractal dimension (D_{HIC}) for four specimens when the SSRT was performed at 27% strain and fracture strain with in situ hydrogen-charging at a 1×10^{-5} s^{-1} strain rates.

Specimens	**G1**	**G2**	**G3**	**G4**
D_{HIC} (27% strain)	0.942 ± 0.011	1.029 ± 0.006	1.137 ± 0.005	0.981 ± 0.009
D_{HIC} (Fracture strain)	1.228 ± 0.004	1.171 ± 0.007	1.137 ± 0.005	1.209 ± 0.004